NASA Technical Memorandum 4602

Mach 10 Computational Study of a Three-Dimensional Scramjet Inlet Flow Field

Scott D. Holland
Langley Research Center • Hampton, Virginia

National Aeronautics and Space Administration
Langley Research Center • Hampton, Virginia 23681-0001

March 1995

Available electronically at the following URL address: http://techreports.larc.nasa.gov/ltrs/ltrs.html

Printed copies available from the following:

NASA Center for AeroSpace Information
800 Elkridge Landing Road
Linthicum Heights, MD 21090-2934
(301) 621-0390

National Technical Information Service (NTIS)
5285 Port Royal Road
Springfield, VA 22161-2171
(703) 487-4650

Summary

The present work documents the computational results for a combined computational and experimental parametric study of the internal aerodynamics of a generic three-dimensional sidewall-compression scramjet inlet configuration at Mach 10. The complete study was designed to demonstrate the utility of computational fluid dynamics (CFD) as a design tool in hypersonic inlet flow fields, to provide a detailed account of the nature and structure of the internal flow interactions, and to provide a comprehensive surface property and flow field database to determine the effects of contraction ratio (CR), cowl position, and Reynolds number (Re) on the performance of a hypersonic scramjet inlet configuration. The work proceeded in several phases: the initial inviscid assessment of the internal shock wave structure, the preliminary computational parametric study, the coupling of the optimized configuration with the physical limitations of the facility, the wind tunnel blockage assessment, and the computational and experimental parametric study of the final configuration. The computational work was used to drive the design of the experimental configuration; the experimental data were then used to validate the computations.

The three-dimensional Navier-Stokes code SCRAMIN was chosen for the computational portion of the study because it uses a well-known and well-proven numerical scheme and has shown favorable comparison with experiment at Mach numbers between 2 and 6. One advantage of CFD was that it provided flow field data for a detailed examination of the internal flow characteristics in addition to the surface properties. The experimental test matrix at Mach 10 included three geometric contraction ratios (3, 5, and 9), three Reynolds numbers (0.55×10^6 per foot, 1.14×10^6 per foot, and 2.15×10^6 per foot), and three cowl positions (at the throat and two forward positions). Computational data for two of these configurations (CR = 3, Re = 2.15×10^6 per foot, at two cowl positions) are presented along with a detailed analysis of the flow interactions in successive computational planes.

Symbols

cpu	central processing unit
CR	geometric contraction ratio, W/g
$C_{x'}$	distance between cowl leading edge and constant-area throat entrance, in.
g	throat gap, in.
H	height of inlet, 4.0 in.
i, j, k	grid coordinate indices
M_e	Mach number at edge of boundary layer
p	static pressure, psia
$p_{t,2}$	pitot pressure, psia
Re	Reynolds number
Re_θ	Reynolds number based on momentum thickness
T	static temperature, °R
$T_{x'}$	distance from sidewall leading edge to throat, 9.5 in.
u,v,w	magnitude of Cartesian velocity components, ft/sec
W	inlet width at sidewall leading edge, in.
x	axial distance measured from baseplate leading edge, in.
x'	local axial distance measured from sidewall leading edge, in.
y	lateral distance across baseplate, measured from centerline toward sidewall, in.
y_{wall}	local inlet width at a given axial station, in.
z	vertical distance from baseplate, measured to complete right-hand set, in.
Z	vertical distance from baseplate, defined for convenience positive down sidewall toward cowl, in.
δ	sidewall compression angle, deg
ζ	spillage angle, deg
η_{ke}	kinetic energy efficiency
Λ	leading-edge sweep angle, deg
ρ	density, $\mathrm{kg/m}^3$

Introduction

The present work documents the computational results for a combined computational and experimental parametric study of the internal aerodynamics of a generic three-dimensional sidewall-compression scramjet inlet configuration at Mach 10. The complete study was designed to demonstrate the utility of computational fluid dynamics as a design tool in hypersonic inlet flow fields, to provide a detailed account of the nature and structure of the flow interactions inside an inlet subject to high Mach number laminar inflow, and to provide a comprehensive surface and flow field database to determine the effects of contraction ratio (CR), cowl position, and Reynolds number (Re) on the performance of a hypersonic scramjet inlet configuration. The work proceeded in several phases: the initial inviscid assessment of the internal shock wave structure, the preliminary computational parametric design study, the coupling of the optimized configuration with the physical limitations of the

facility, the wind tunnel blockage assessment, and the computational and experimental parametric study of the final configuration. The purpose of the present work is to present the computational parametric results. The complete experimental database (ref. 1), which included 256 channels of pressure data (including static pressure orifices, pitot pressures, and entrance and exit flow rakes) along with oil flow and infrared thermography, provided a detailed experimental description of the flow over contraction ratios of 3, 5, and 9, Reynolds numbers of 2.15×10^6 per foot, 1.14×10^6 per foot, and 0.55×10^6 per foot, and three cowl positions. The entire experimental test matrix is not duplicated; rather, performance parameters and detailed discussions of the flow in successive computational planes are presented for two configurations: CR = 3, Re = 2.15×10^6 per foot, with the cowl located at the throat entrance and also halfway between the sidewall leading edge and the throat entrance. Because this document is intended primarily as a data release, the reader is directed to the primary document (ref. 2) for the overview and discussion of the entire program with comparative computational and experimental results.

Extensive study has been devoted to the three-dimensional sidewall-compression scramjet inlet for a variety of test conditions, both computationally and experimentally, for high Mach number air-breathing propulsion applications. (See, for example, refs. 3 to 16.) This concept (see fig. 1) makes use of the forebody bow shock wave, which precompresses the flow in the vertical direction upstream of the inlet entrance. The three-dimensional sidewall-compression scramjet inlet (fig. 2) accomplishes further compression in the horizontal direction. The leading edges of these wedge-shaped sidewalls are swept both to reduce the aerothermal loads on the leading edge and to provide a window for spillage at the lower Mach numbers to aid in starting the inlet. The sweep has the effect of turning the flow away from the forebody plane, leading to a decrease in mass capture due to flow spillage. As the Mach number is increased, the sidewall shock wave angles become smaller, effectively partially closing that spillage window and increasing the mass capture, thereby making the inlet more efficient at higher Mach numbers. These characteristics make it possible to consider a fixed geometry inlet for use over a wide Mach number range.

The past two decades have brought tremendous advances in numerical methods and in computer hardware development that have created an enhanced capability for calculating increasingly more complicated flow fields. Computational fluid dynamics (CFD) is now used in certain applications as an engineering design tool. One advantage of computational fluid dynamics is that it provides flow field data, where experimental data is typically limited to surface measurements or global flow field measurements. White, Drummond, and Kumar (ref. 17) point out the utility of CFD for providing parametric studies in a timely and cost-effective manner, and once wind tunnel data is obtained, aiding in the explanation of unusual or unexpected phenomena by giving detailed flow field data. Additionally, the ability of the code to match the surface measurements obtained experimentally gives the designer greater confidence in the computed flow field data and in the possibility of using the code to extrapolate outside the range of test conditions available experimentally.

The complete study (discussed in ref. 2) uses CFD in this design and analysis capacity. Because instrumented wind-tunnel models are quite expensive, a computational parametric study (reported in ref. 18) was performed to minimize the costs of fabrication by eliminating from consideration designs which promised poor performance. The results of that trade-off study led to the selection of a configuration with 45° leading-edge sweep for further computational and experimental study. Prior to construction of the highly instrumented model, an inexpensive experimental wind tunnel blockage model was fabricated to determine the effect of the size of the model on the performance of the facility (ref. 9). Despite the fact that the maximum cross-sectional area of the model exceeded 30 percent of the inviscid test core, no evidence of tunnel blockage was noted, based on pitot pressure measurements of the free-stream and static pressures along the tunnel sidewall. A highly instrumented wind tunnel model then was fabricated and tested in the Langley 31-Inch Mach 10 Tunnel; a concurrent computational study was performed to provide a direct comparison between computation and experiment for the configuration derived from the aforementioned design process.

The present work provides a detailed presentation of the CFD data set for two configurations from the combined computational and experimental parametric investigation of the internal aerodynamics of a generic three-dimensional sidewall-compression scramjet inlet at Mach 10 (ref. 9). Although geometrically simple, inlets of this genre generate a very complicated flow field, in which corner flow, shock-induced separation, and shock-shock/shock-boundary-layer interactions are among the flow characteristics. Each of these issues have been addressed separately by other researchers (e.g., refs. 19 to 27), but the desired result of the interactions generated by the inlet is the creation of an efficiently compressed, supersonic flow at the combustor face. The prediction of such complicated flow fields is of particular interest to vehicle designers and analysts for whom high local pressure gradients and high heating influence the

total aerodynamic and structural design of the flight vehicle.

A discussion of the computational methods employed for the study is presented. Then a comparison of the global flow features as well as performance parameters for the 0 percent and 50 percent cowl configurations at CR = 3 and Re = 2.15×10^6 per foot are presented. The axial progression of internal interactions is detailed in several computational planes in the appendix.

Computational Methods

The three-dimensional Reynolds-averaged Navier-Stokes code SCRAMIN of reference 12 was adapted for the present study because it uses a well-known and well-proven numerical scheme and has shown favorable comparison with experiment at lower Mach numbers (2 to 6, which, as a result of this study, can be extended to 10). The code solves the three-dimensional Navier-Stokes equations in full-conservation form by using MacCormack's time-accurate, explicit predictor-corrector method (ref. 28). This method is second-order accurate in time and space and yields to a high degree of vectorization. The present work makes use of an algebraic grid-generation technique with grid clustering (ref. 29) in lateral and vertical directions near boundaries.

Configuration Description

The leading-edge sweep Λ and the sidewall compression angle δ were fixed at 45° and 6°, respectively. (See fig. 2.) The forebody plane was represented by a flat plate, which extended 9 in. upstream of the inlet entrance plane. The inlet sidewalls were 4.0 in. tall with a total length of 21 in. The sidewalls were mounted on a 30-in-long flat plate (referred to as the baseplate) which provided the inflow laminar boundary layer. A photograph of the experimental inlet model is presented in figure 3.

The geometric contraction ratio (CR) was defined as the ratio of the inlet entrance width to the throat gap W/g (fig. 2). The cowl position was defined by the forward extent of the cowl leading edge ahead of the throat ($C_{x'}$, fig. 2) as a percentage of the distance to the throat ($T_{x'}$). Thus, when the cowl was moved forward halfway between the beginning of the throat and the sidewall leading edge, it was termed 50 percent cowl ($C_{x'}/T_{x'} = 0.50$) ; when the cowl was located at the throat, it was termed 0 percent cowl ($C_{x'}/T_{x'} = 0.00$).

Computational Flow Conditions and Test Matrix

Two representative experimental configurations were selected for the computational study: 0 percent cowl position and 50 percent cowl position, both of which have CR = 3 and Re = 2.15×10^6 per foot. Flow conditions for the computational study were obtained from the Mach 10 wind tunnel flow conditions. Expanding the flow to Mach 10 at a free-stream unit Reynolds number of 2.15×10^6 per foot yielded a very low free-stream static pressure (0.03 psia). The free-stream static temperature was 50 K. The inlet flow field was computed based on the assumption of laminar flow.

Computational Grid

The computational grid for the configuration is presented in figure 4. Because the configuration is symmetric, only half the inlet is shown; i.e., half the baseplate and one sidewall are shown. The lateral scale has been exaggerated by a factor of 2 in order to more clearly view the interactions. The mesh has 86 grid points in the axial direction, 31 laterally, and 61 vertically (46 inside the inlet and 15 underneath—not shown—for the flow spillage). The grid is swept at the leading-edge sweep angle to better resolve interactions which occur in planes of constant leading-edge sweep. The sidewall leading edge is located at $i = 30$ and mounts to the forebody plane (baseplate) 9 in. aft of the baseplate leading edge. The constant-area throat begins at $i = 55$ (9.5 in. aft of the sidewall leading edge); the shoulder is also swept at the leading-edge sweep angle. The exit of the constant-area throat is a vertical plane located at $i = 72$, 25 in. aft of the baseplate leading edge. As indicated in figure 4, the inlet throat is longer near the baseplate than at the cowl plane because of the difference in sweep of the throat entrance and exit. In order to accommodate the swept throat entrance and vertical exit, the grid is linearly transitioned from swept to vertical in this region. The aft expansion added to the wind tunnel model to minimize tunnel blockage and to accommodate the rake mechanism was also modeled in the $i = 72$ to 86 region. The entire model was 30 in. long. After the desired grid was obtained, a final check on grid independence was performed by increasing the grid density by 50 percent in all three coordinate directions. Aside from a substantial increase in cpu time, no influence of the grid refinement was noted on the engineering accuracy of the pressure distributions. Comparison plots of the centerline pressure distributions for each grid along with experimental data are presented in reference 2. The residual typically dropped five orders of magnitude in the convergence process.

Boundary and Initial Conditions

Because shock/boundary-layer interactions depend on the size and character of the incoming boundary layer, the inflow boundary was maintained at free-stream conditions and therefore a laminar boundary layer developed naturally on the 9 in. of flat plate upstream of the inlet entrance. An extrapolation boundary condition was applied at the exit plane. On solid surfaces, all velocity components as well as the normal pressure gradient are required to vanish. A constant temperature distribution (300 K) provided the thermal boundary condition. Open boundaries were calculated assuming vanishing normal gradients in velocity, temperature, and pressure. Because the flow field was symmetric, only half the field was computed and symmetry boundary conditions were imposed. The initial conditions were given by assigning free-stream conditions to each grid point, except at the boundaries, where appropriate boundary conditions were applied. The leading edges of all surfaces were modeled as theoretically sharp.

Results and Discussion

The computational grid for the configuration is presented in figure 4. Recall that the lateral scale has been exaggerated by a factor of 2 to more clearly view the interactions. For convenience, plots of computational (i = Constant) planes are overlaid with reference lines dividing the inlet height and local width into 10 evenly spaced segments. In each of these planes, the inlet centerline is the right boundary and the inlet sidewall is the left boundary. Thus, y/y_{wall} increases from 0 to 1 from right to left on the figures. Additionally, the baseplate is at the top and the cowl at the bottom, so that Z/H goes from 0 to 1 from the top of the page to the bottom. (The right-hand coordinate system requires that z be negative measured down the sidewall; consequently, Z is introduced for convenience as the negative of z and is therefore measured as the positive distance from the baseplate toward the cowl.) Pressure contours, cross-flow velocity vectors, and particle traces are used to identify shock wave locations, separation regions, and flow streamlines. Simulated oil flows are generated by restricting the particle traces to a two-dimensional plane, with velocities one grid point away from the wall.

Because each computation requires a significant expenditure of cpu time, the entire experimental test matrix of reference 1 is not duplicated. Because of the large number of plots required to fully document the flow fields, shock interactions and internal vortices evident in the i = Constant planes are discussed in more detail in the appendix. Brief discussions of the internal shock interactions are presented for the CR = 3 configuration at Re = 2.15×10^6 per foot for 0 percent and 50 percent cowl positions. The performance of both configurations is then assessed and compared in terms of mass capture, average throat Mach number, total pressure recovery, and average inlet compression.

To assess the validity of the assumption of a laminar inlet inflow, the laminar-boundary-layer thickness (based on 99.5 percent of the edge velocity), the displacement thickness, and the inflow momentum thickness were calculated at the inlet entrance station and were found to be 0.35 in. (approximately 9 percent of the inlet height), 0.20 in., and 0.0076 in., respectively, yielding a Reynolds number based on momentum thickness Re_θ of 1361.6. The equation Re_θ/M_e = Constant was shown by Tauber (ref. 30) to be an approximate empirical correlation of measurements for supersonic or hypersonic boundary-layer transition. The constant for transition varies between 150 and 350 depending upon the ratio of roughness height to momentum thickness, among other parameters. For Mach 10 inflow, the Re = 2.15×10^6 per foot test condition yielded a value of $\text{Re}_\theta/M_e = 136$, which is less than the value for transition. Additionally, past experience in the wind tunnel in which the experimental portion of the work was performed indicates that a laminar flow on the forebody plate would be expected.

0 Percent Cowl and 50 Percent Cowl Configurations

Contours of p/p_∞ at three heights within the inlet (Z/H = 0.25, 0.50, and 0.75) are presented in figures 5(a), (b), and (c), respectively, for the 0 percent cowl with CR = 3 and Re = 2.15×10^6 per foot. The shock wave generated from the sidewall leading edge reaches the centerline at approximately 69 percent of the distance between the leading edge and the throat entrance ($x'/T_{x'} = 0.69$) and then impinges on the sidewall just aft of the shoulder (throat entrance). In the horizontal center plane (fig. 5(b)), the shock wave is observed to reflect from the sidewall, reaching approximately the centerline at the exit plane. It is important to note that because the length of the constant-area throat varies with vertical position in the inlet (see fig. 4), the position of the shock wave at the exit plane varies as a function of Z/H. For example, at Z/H = 0.25 (fig. 5(a)), the shock wave appears to have reached the centerline just ahead of the exit plane; the shock wave is located very near the centerline of the inlet for the midheight (fig. 5(b)); and the shock wave has not quite reached the centerline nearest the cowl (fig. 5(c)). A similar set of contour plots for the 50 percent cowl configuration is presented in figure 6. A comparison of these plots with those of figure 5 indicates that in these three planes, the shock wave structure is unchanged by the forward movement of the cowl. Only a small increment in pressure is

Table I. Summary of Computed Inlet Performance Parameters

Configuration	η_{ke}	Mass capture, percent	Exit Mach number	Total pressure recovery	$p_{t,2}/p_\infty$	p/p_∞
0 percent cowl	99.2	93.4	6.3	0.61	361.6	9.2
50 percent cowl	98.8	98.0	6.0	0.48	353.0	9.7

noted in the throat region at $Z/H = 0.75$. This is borne out by comparison of the sidewall and baseplate pressure contours for the 0 percent and 50 percent cowl configurations in figures 7 and 8, respectively, where the shock wave emanating from the cowl leading edge at the 50 percent cowl position appears to influence the $Z/H = 0.75$ station approximately at the throat. Compression of up to $p/p_\infty = 10.75$ is observed in the cowl-sidewall corner upstream of the throat entrance. Aft of the sidewall shock impingement, there appear to be only slight changes in the throat region. The region beneath $Z/H = 0.75$ is dominated by pressure ratios of approximately 20, compared with 15 for the 0 percent cowl. This difference accounts for the slight increase (5 percent) in average exit plane compression from 9.203 for 0 percent cowl to 9.698 for 50 percent cowl (table I). Among the noteworthy interactions demonstrated in these figures are the viscous interaction near the sidewall leading edge (pressure rise and fall), the shock impingement aft of the shoulder, the expansion of the flow around the shoulder (particularly evident on the baseplate aft of the shoulder), and the cowl shock wave near the bottom of the figure. (These features are evident in greater detail in the appendix, where the flow features in several successive i = Constant planes are detailed.)

Comparison of sidewall pressure distributions with the symmetry plane pressure contours (figs. 9 and 10) for 0 percent and 50 percent cowls, respectively, permits reconstruction of the swept oblique shock trains. The first centerline shock interaction is observed to have a slightly irregular shape at $Z/H \approx 0.5$ because of the effects of the weak compression formed on the baseplate leading edge due to the displacement effects of the boundary-layer growth. These centerline contours (fig. 10) indicate that the domain of influence of the forward cowl is limited. While the cowl shock wave appears to remain intact through the first glancing-shock–centerline interaction, the second interaction appears to dominate, and much of the explicit effects of the cowl shock wave vanish upstream of the exit plane. Although the cowl shock wave in the cowl forward position has the potential to influence more of the exit plane, the aft cowl produces higher pressures (due in part to the fact that the shock wave is stronger and turns the flow at a greater angle) over a slightly smaller vertical extent into the exit plane, which tends to cancel out much of the expected increase in average compression at the exit plane.

Regions of streamwise flow separation are indicated in figures 11 and 12 by means of contours of negative axial velocity. The glancing shock wave is observed to separate the baseplate boundary layer both upstream and downstream of the centerline interaction. A comparison between the 0 percent and 50 percent cowl configurations indicates that the separation along the sidewall impingement line (aft of the shoulder) is enhanced by the presence of the cowl shock wave in the lower 25 percent of the inlet. While the forward extent is increased on the sidewall, the separation in the cowl-sidewall corner at the throat entrance ($x'/T_{x'} = 1.00$) is greatly diminished.

Interactions on the inlet sidewall are also presented by way of sidewall and baseplate particle traces (figs. 13 and 14). By restricting the particles to their respective planes, a simulated oil flow is created. The shock impingement in particular is evident. It is also observed that in the uppermost 25 percent of the inlet, the sidewall flow patterns indicate an upward movement until the flow separates on the sidewall (denoted by the accumulation line) in the immediate vicinity of the sidewall-baseplate juncture. (This separation and reattachment are demonstrated in the v, w velocity vector plots in the appendix.) Diverging streamlines on the baseplate indicate a flow reattachment. This pattern is typical of what Kubota and Stollery (ref. 19) referred to as an induced layer. (Cross-flow velocity vectors in i = Constant planes presented in the appendix indicate multiple vortical patterns in the upper 20–30 percent of the inlet that result from this induced cross flow.) A downward component exists over much of the sidewall. This flow downturning is expected based on the swept shock structure, which dictates an increase in downturning with each swept, reflected internal shock wave. Near $Z/H = 1.0$, the sidewall streamlines are observed to turn downward more sharply as the compressed flow expands downward into the free stream. This turning is more severe in the low-momentum boundary layer, leading to a highly skewed, helical velocity distribution in the boundary layer.

The location of the cowl is observed to have no effect on the upper half of the inlet. Forward of the cowl

at $Z/H = 1.00$, the strong flow downturning caused by the expansion of the compressed flow into the free stream for the 0 percent cowl configuration (fig. 13) is interrupted by the presence of the cowl, which prevents the flow spillage and further compresses the flow. A corner flow is observed to develop in the sidewall-cowl corner much like that of the baseplate-sidewall corner, with lines of separation, reattachment, and upstream influence evident. (In this case, the cowl plate is viewed as the fin interacting with the boundary layer established on the sidewall.)

The static pressure distribution in the exit plane is presented in figures 15 and 16. The cowl shock wave is observed to influence the bottom 15 percent of the throat. The pressure distribution in the upper 40 percent of the exit plane is constant at $p/p_\infty \approx 7$. The forward placement of the cowl has little effect on the nonuniformity of the exit plane compared with the 0 percent cowl configuration (fig. 15) because of the dispersion of the cowl shock wave by the internal reflecting shock waves. The magnitudes of the pressures show only a nominal increase near the cowl; however, this small pressure augmentation affects the lower 40 percent of the inlet, yielding an expected increase in average compression. A comparison of the exit plane Mach number plots (fig. 17 for 0 percent cowl and fig. 18 for 50 percent cowl) further supports the limited domain of influence of the cowl and indicates that the inlet is started (established supersonic flow throughout the inlet). The mechanisms leading to the vertical and horizontal nonuniformity in the exit plane (including the induced cross flow and the effects of the sidewall-boundary-layer thickness in further constricting the throat) are plotted in the appendix.

Cowl Position Effects on Inlet Performance

A global comparison of cowl position effects indicates that the primary changes in the flow structure are localized and do not have a strong effect on the average exit plane flow quantities. The performance of the inlet was compared through the use of momentum-weighted and area-weighted quantities, for which the definitions have been provided in reference 16. Table I shows the performance parameters for both configurations and indicates that the primary effect of moving the cowl forward is to capture more of the downturned flow which would have otherwise spilled out ahead of the cowl. The mass capture is observed to increase from 93.4 to 98.0 percent. The momentum-averaged exit Mach number decreases slightly from 6.3 to 6.0 because the cowl shock wave affects a larger percentage of the exit area for the 50 percent cowl configuration. The effects of the cowl shock wave also cause a decrease in the momentum-averaged total pressure recovery from 0.61 to 0.48 and in kinetic energy efficiency η_{ke} from 99.24 to 98.82 percent. Likewise the area-averaged pitot pressure ratio ($p_{t,2}/p_\infty$) decreases slightly from 361.6 to 353.0. A slight increase in area-averaged inlet compression (static pressure ratio, p/p_∞) is also observed, from 9.20 to 9.73. The most dramatic effect is an increase of nearly 5 percent in inlet mass capture, at a cost of decreased total pressure recovery.

Conclusions

The present work documents the computational results for a combined computational and experimental parametric study of the internal aerodynamics of a generic, three-dimensional sidewall-compression scramjet inlet configuration at Mach 10. The complete study was designed to demonstrate the utility of computational fluid dynamics as a design tool in hypersonic inlet flow fields, to provide a detailed account of the nature and structure of the internal flow interactions, and to provide a comprehensive surface property and flow field database to determine the effects of contraction ratio, cowl position, and Reynolds number on the performance of a hypersonic scramjet inlet configuration. A summary of the global flow-field interactions and performance parameters was presented by way of comparison between the 0 and 50 percent cowl positions for a contraction ratio of 3 and a Reynolds number of 2.15×10^6 per foot.

The conclusions may be summarized as follows:

1. The inlet is started (i.e., has established supersonic flow in the throat) for both configurations.

2. Each swept internal shock wave encountered by the flow enhances the local flow downturning (spillage angle).

3. Significant vertical flow nonuniformity in exit plane (i.e., Mach number and mass flux deficits in the upper 20–30 percent of the inlet height) is traced to the cross-flow-induced vorticity.

4. Interaction between the internal reflecting shock wave and the cowl shock wave tends to disperse the latter. Although the cowl shock wave in the cowl forward position has the potential to influence more of the exit plane, the aft cowl produces higher pressures (partly because the shock wave is stronger and turns the flow at a greater angle) over a slightly smaller vertical extent into the exit plane, which tends to limit the expected augmentation in average compression at the exit plane.

5. The forward cowl increases the lateral and vertical extent of the separation along the sidewall shock impingement, while greatly diminishing the separation in the cowl/sidewall corner.

6. In terms of performance, primary changes in the flow structure due to cowl position appear to be localized and do not have a strong effect on the average exit plane flow quantities. The most dramatic influence on inlet performance due to a forward cowl position was an increase in mass capture of nearly 5 percent (from 93.4 to 98.0 percent). Slight decreases in exit Mach number (from 6.3 to 6.0) and kinetic energy efficiency (from 99.2 to 98.8 percent) and an increase in average compression (from 9.2 to 9.7) were also noted.

7. Finally, a typical contour plot of pressure in the exit plane reveals a compressed core which is somewhat buffered from the baseplate and cowl by a low-momentum region that results from the induced cross flows. Thus the baseplate pressure alone does not necessarily yield a good quantitative indication of the compression of the core flow. Sidewall and flow field measurements are therefore required for the validation of inlet performance calculations.

NASA Langley Research Center
Hampton, VA 23681-0001
December 23, 1994

Appendix

Cowl Position Effects on Internal Flow Structure

Six computational (i = Constant) planes are used to track the axial progression of the internal flow interactions for both the 0 and 50 percent cowl configurations. To allow for easier examination of the data, the lateral dimension has also been expanded by a factor of 2 for all plots in the appendix. The planes up to the throat are inclined at the leading-edge sweep angle and are linearly transitioned in the constant-area throat region to the vertical exit plane. The sidewall leading edge is located at plane $i = 30$, the throat is at plane $i = 55$, and the exit is at plane $i = 72$. (Recall from fig. 4 that the expansion aft of the constant-area throat was modeled in the $i = 72$ to $i = 86$ region. This expansion was included in the design of the experimental test article to minimize wind-tunnel blockage and was included in the computations solely to match the exact wind-tunnel configuration; computational data from this region are therefore not presented.) The positions of the planes ahead of the throat are identified in terms of $x'/T_{x'}$, i.e., the location of the plane as a fraction of the distance between the leading edge and the entrance of the constant-area throat. To orient the reader, a composite of pressure contours in the six i = Constant planes in a perspective sketch of the inlet is first presented, followed by a similar composite of v, w velocity vectors. An expanded view of the pressure contours and velocity vectors in each plane is then presented to develop the internal flow structure for the 0 percent cowl configuration. A similar set of figures is also presented for the 50 percent cowl configuration to examine the explicit effects of a forward cowl placement on this fixed geometry inlet.

Internal Inlet Flow Structure

A composite of the p/p_∞ contours in the six i = Constant computational planes is presented in figure 19, and a composite of the v, w velocity vectors, in figure 20. Contours of p/p_∞ and v, w velocity vectors are presented in a expanded form for easier examination in figures 21 and 22, respectively. Both sets of plots are overlaid with reference lines which divide the domain into 10 evenly spaced segments.

Figures 21(a), (b), and (c) show the p/p_∞ contours in i = Constant planes upstream of the throat and indicate that the shock wave remains nominally planar through the interaction at the centerline. The weak compression formed as a result of the boundary-layer growth at the baseplate leading edge is denoted by the horizontal contour bands at approximately $Z/H = 0.40$. (Recall that the forebody plane is located $Z/H = 0.0$ and the cowl plane is at $Z/H = 1.0$.) The expansion of the compressed flow into the free stream beneath the inlet is also noted. This turning is observed to be most severe in the lower momentum region of the sidewall boundary layer (see the velocity vectors in fig. 22), leading to a helical boundary-layer profile near the bottom of the inlet. A slight expansion is observed in the immediate vicinity in the sidewall/baseplate corner, and the velocity vectors indicate that this expansion of the compressed flow induces a cross flow across the baseplate. (Kubota and Stollery (ref. 19) have also observed this interaction and refer to it as an induced layer.) With increasing distance into the inlet, this cross flow extends to the centerline and subsequently forms multiple recirculations.

Pressure contours aft of the cowl leading edge (figs. 21(d), (e), and (f)) indicate that the domain of influence of the cowl is limited to approximately the lower 25 percent of the inlet height. Velocity vectors in that same region (figs. 22(d), (e), and (f)) show that a corner flow develops in the sidewall/cowl corner much like that of the baseplate/sidewall corner. Separation, reattachment, and upstream influence are shown in figure 13. (In this case, the cowl plate is viewed as a fin interacting with the boundary layer established on the sidewall.) The large vortical structures in the upper 25 percent of the inlet which develop as a result of the induced cross flow are responsible for the significant mass flux deficit in that region (compare fig. 22(f) with fig. 23, which shows contours of mass flux ρu in the exit plane).

Effects of Forward Cowl Placement on Flow Structure

Figures 24 and 25 present composites of the internal compression (p/p_∞) and v, w velocity vectors, respectively, in six cross-flow planes for the CR = 3, 50 percent cowl configuration at a unit free-stream Reynolds number of 2.15×10^6 per foot. These i = Constant planes are presented individually in figures 26(a) to (f) (p/p_∞) and figures 27(a) to (f) (v, w velocity vectors). It is evident from comparison of these figures with the figures from the 0 percent cowl configuration that the effects of the forward cowl placement are limited to the lower half of the inlet. At the throat entrance plane $i = 55$, the pressure contours (fig. 26(d)) indicate that the interaction between the cowl shock wave and the sidewall shock wave tends to disperse the cowl shock wave. Velocity vectors in this plane (fig. 27(d)) reveal recirculation regions under the cowl shock wave similar to the induced layer formed in the sidewall/baseplate juncture.

The cowl shock wave is difficult to identify explicitly in the pressure contours (fig. 26(f)) in the exit plane

(i = 72). The multiple interactions with the sidewall shock wave have significantly obscured its effects. The maximum pressure in the exit plane is less than for the 0 percent cowl configuration (fig. 21(f)); however, the size of the region augmented by the cowl shock wave is much larger. Velocity vectors (fig. 27(f)) again indicate that the corner vortices have survived the sidewall shock wave. Figure 28 indicates significant momentum deficits in the upper 25 percent of the inlet and in the sidewall boundary layer near the cowl.

The sidewall shock waves have a detrimental effect on the cowl shock wave, tending to obscure and disperse its compression. Although the 50 percent cowl configuration has the greatest potential to influence the exit plane (simply because the inviscid cowl shock wave would be expected to affect a greater fraction of the exit plane), it encounters more sidewall shock interactions which tend to cancel out this effect. On the other hand, the 0 percent cowl is observed to generate a stronger shock wave because of a stronger local downturning at the cowl leading edge, and, although it does not reach as far up into the inlet at the exit plane, the cowl shock wave encounters fewer reflected shock waves. The combination of these effects leads to the observation that the forward cowl has a smaller impact on the average exit parameters than might be expected. The maximum pressure in the exit plane is lower for the 50 percent cowl configuration, but the area affected by the pressure augmentation is much larger, leading to a net increase in average compression. As previously noted, the principal benefit of the cowl forward configuration is the increased mass capture.

References

1. Holland, Scott D.: *Mach 10 Experimental Database of a Three-Dimensional Scramjet Inlet Flow Field.* NASA TM-4648, 1995.

2. Holland, Scott D.: *Internal Aerodynamics of a Generic Three-Dimensional Scramjet Inlet at Mach 10.* NASA TP-3476, 1995.

3. Trexler, C. A.: Performance of an Inlet for an Integrated Scramjet Concept. *J. Aircr.*, vol. 11, Sept. 1974, pp. 589–591.

4. Trexler, C. A.: Inlet Performance of the Integrated Langley Scramjet Module (Mach 2.3 to 7.6). AIAA-75-1212, Sept.–Oct. 1975.

5. Trexler, Carl A.; and Souders, Sue W.: *Design and Performance at a Local Mach Number of 6 of an Inlet for an Integrated Scramjet Concept.* NASA TN D-7944, 1975.

6. Kanda, Takeshi; Komuro, Tomoyuki; Masuya, Goro; Kudo, Kenji; and Murakami, Atsuo: Mach 4 Testing of Scramjet Inlet Models. AIAA-89-2680, July 1989.

7. Trexler, Carl A.: *Tests of Two Sidewall-Compression Scramjet Inlets at Mach 18.1 to 21.6 in Helium.* NASP TM-1018, NASP JPO, Wright-Patterson AFB, 1988.

8. Holland, Scott D.; and Perkins, John N.: Mach 6 Testing of Two Generic Three-Dimensional Sidewall Compression Scramjet Inlets in Tetrafluoromethane. AIAA-90-0530, Jan. 1990.

9. Holland, Scott D.; Hodge, Jeffrey S.; and Perkins, John N.: Wind Tunnel Blockage Study of a Generic Three-Dimensional Sidewall Compression Scramjet Inlet at Mach 10. AIAA-91-0294, Jan. 1991.

10. Holland, Scott Douglas: A Computational and Experimental Investigation of a Three-Dimensional Hypersonic Scramjet Inlet Flow Field. Ph.D. Thesis, North Carolina State Univ., Mar. 1991.

11. Vinogradov, V. A.; Stepanov, V. A.; and Aleksandrovich, E. V.: Numerical and Experimental Investigation of Airframe-Integrated Inlet for High Velocities. AIAA-89-2679, July 1989.

12. Kumar, Ajay: *Numerical Simulation of Scramjet Inlet Flow Fields.* NASA TP-2517, 1986.

13. Kumar, Ajay; and Trexler, Carl A.: Analysis and Performance Prediction of Scramjet Inlets Utilizing a Three-Dimensional Navier-Stokes Code. *Langley Symposium on Aerodynamics—Volume 1*, Sharon H. Stack, compiler, NASA CP-2397, 1986, pp. 187–208.

14. Srinivasan, S.; McClinton, C. R.; and Kamath, P. S.: *Numerical Simulation of Flow Through the Langley Parametric Scramjet Engine.* SAE Tech. Paper Ser. 892314, Sept. 1989.

15. Sekar, B.; Thomas, S.; and Srinivasan, S.: A Numerical Parametric Study of a Scramjet Inlet in a Mach 6 Arc Heated Test Facility. AIAA-90-0531, Jan. 1990.

16. Kumar, Ajay; Singh, D. J.; and Trexler, Carl A.: Numerical Study of the Effects of Reverse Sweep on Scramjet Inlet Performance. *J. Propuls. & Power*, vol. 8, no. 3, 1992, pp. 714–719.

17. White, M. E.; Drummond, J. P.; and Kumar, A.: Evolution and Application of CFD Techniques for Scramjet Engine Analysis. *J. Propuls. & Power*, vol. 3, 1987, pp. 423–439.

18. Holland, Scott: *Computational Parametric Study of Sidewall-Compression Scramjet Inlet Performance at Mach 10.* NASA TM-4411, 1993.

19. Kubota, H.; and Stollery, J. L.: An Experimental Study of the Interaction Between a Glancing Shock Wave and a Turbulent Boundary Layer. *J. Fluid Mech.*, vol. 116, 1982, pp. 431–458.

20. Garrison, T. J.; Settles, G. S.; Narayanswami, N.; and Knight, D. D.: Structure of Crossing-Shock Wave/Turbulent Boundary-Layer Interactions. AIAA-92-3670, July 1992.

21. Panaras, Argyris G.; and Stanewsky, Egon: Numerical Study of Secondary Separation in Glancing Shock/Turbulent Boundary Layer Interactions. AIAA-92-3666, July 1992.

22. Degrez, G.; and Ginoux, J. J.: Three-Dimensional Skewed Shock Wave Laminar Boundary Layer Interaction at Mach 2.25. AIAA-83-1755, July 1983.

23. Stainback, P. Calvin; and Weinstein, Leonard M.: *Aerodynamic Heating in the Vicinity of Corners at Hypersonic Speeds.* NASA TN D-4130, 1967.

24. Knight, Doyle D.; Horstman, C. C.; and Settles, Gary S.: Three-Dimensional Shock Wave-Turbulent Boundary Layer Interactions Generated by a Sharp Fin at Mach 4. AIAA-92-0648, Jan. 1991.

25. Narayanswami, Natraj: A Numerical Investigation of the Interaction Between Crossing Oblique Shocks and a Turbulent Boundary Layer. Ph.D. Thesis, Rutgers–The State Univ., May 1992.

26. Settles, Gary S.; and Dolling, David S.: Swept Shock-Wave/Boundary-Layer Interactions. *Tactical Missile Aerodynamics—General Topics*, AIAA, 1992, pp. 505–574.

27. Settles, G. S.; and Dolling, D. S.: Swept Shock/Boundary-Layer Interactions—Tutorial and Update. AIAA-90-0375, Jan. 1990.

28. MacCormack, R. W.: The Effect of Viscosity in Hypervelocity Impact Cratering. AIAA-69-354, Apr.–May 1969.

29. Roberts, Glyn O.: Computational Meshes for Boundary Layer Problems. *Proceedings of the Second International Conference on Numerical Methods in Fluid Dynamics.* Volume 8 of Lecture Notes in Physics, Maurice Holt, ed., Springer-Verlag, 1971, pp. 171–177.

30. Tauber, M. E.: *A Brief Review of Some Mechanisms Causing Boundary Layer Transition at High Speeds.* NASA TM-102834, 1990.

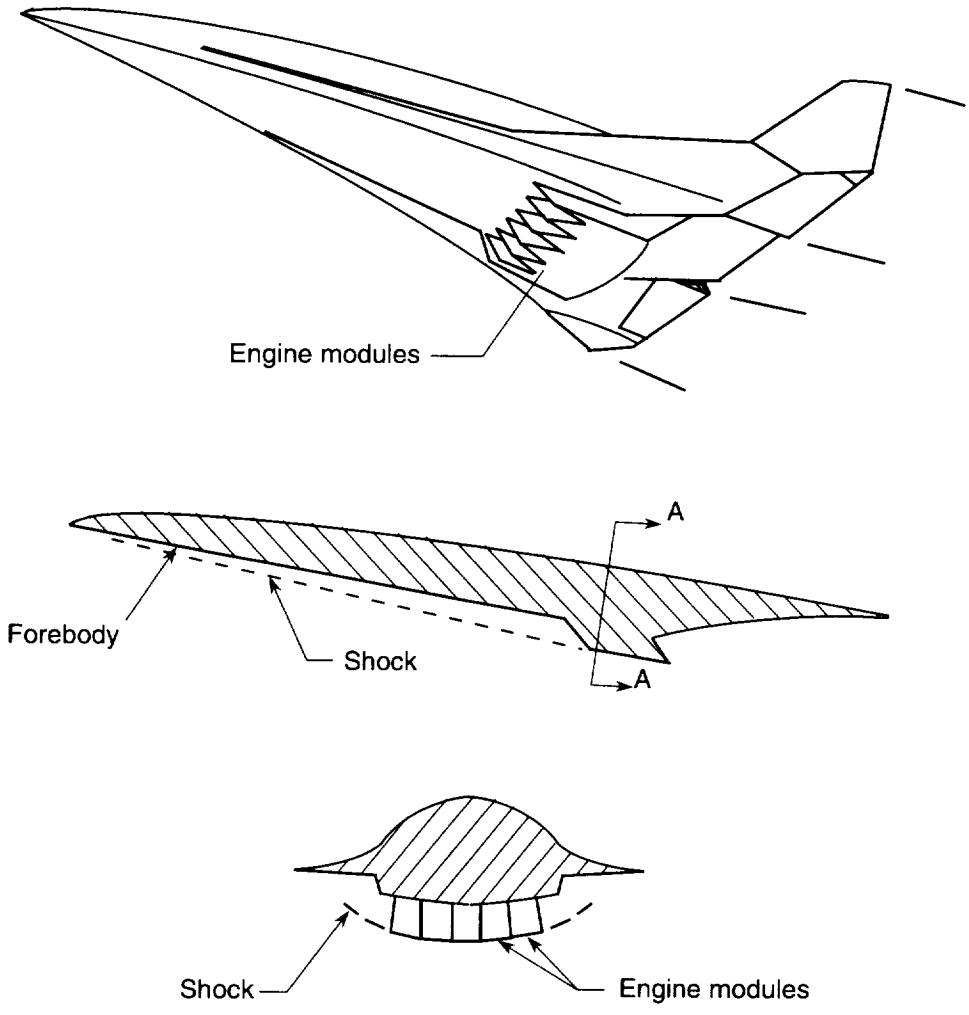

Figure 1. Propulsion airframe integration.

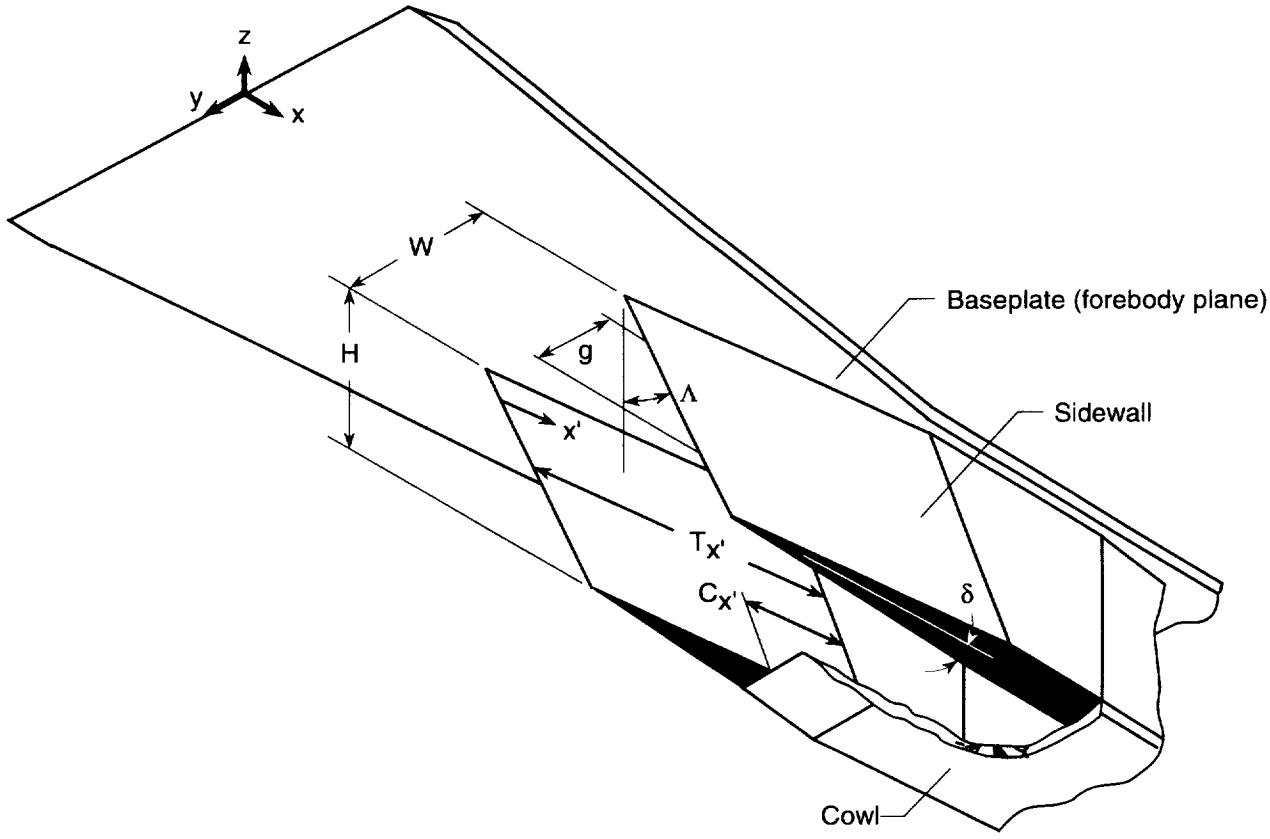

Figure 2. Inlet model shown in flight orientation.

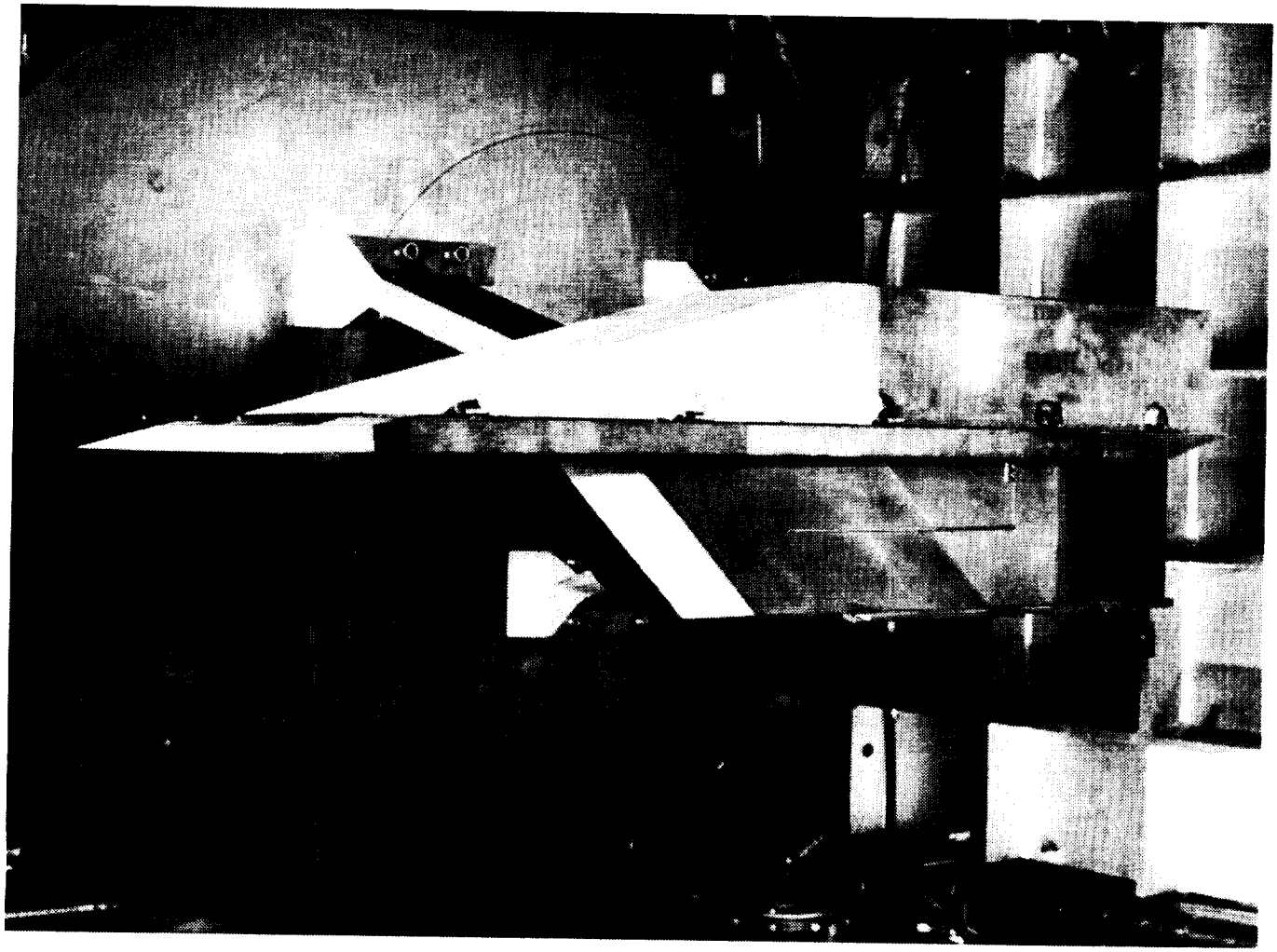

L-90-04394

Figure 3. Photograph of inlet model on injection plate.

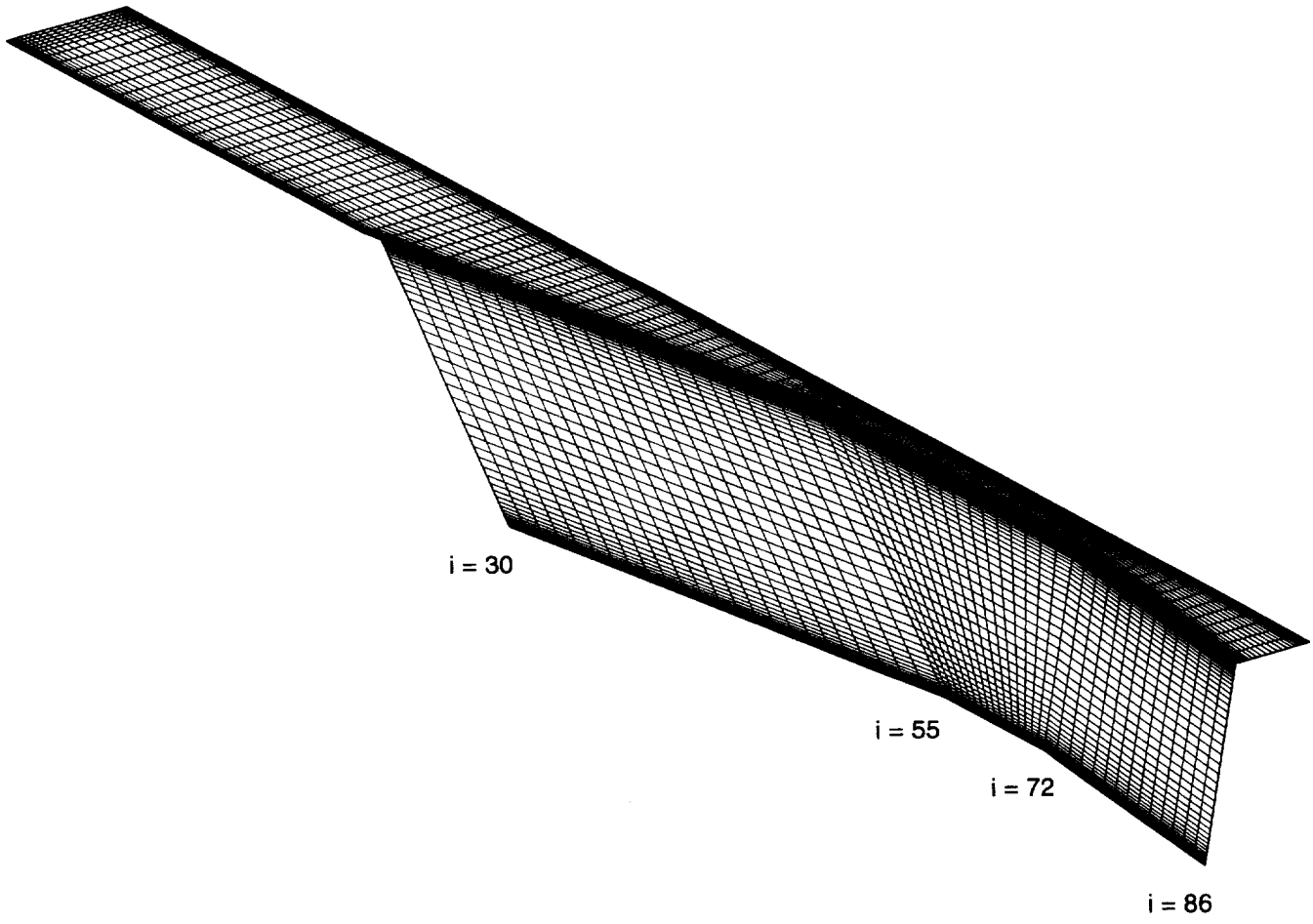

Figure 4. Computational grid of inlet sidewall and baseplate surfaces.

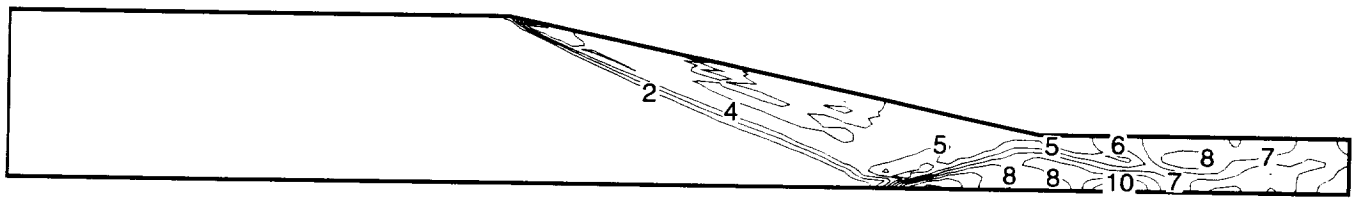

(a) $Z/H = 0.25$.

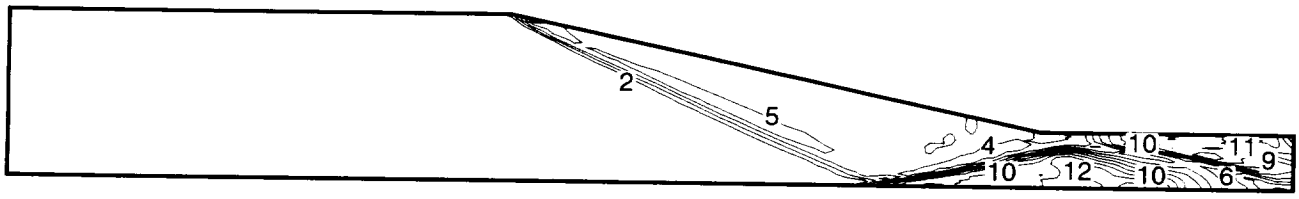

(b) $Z/H = 0.50$.

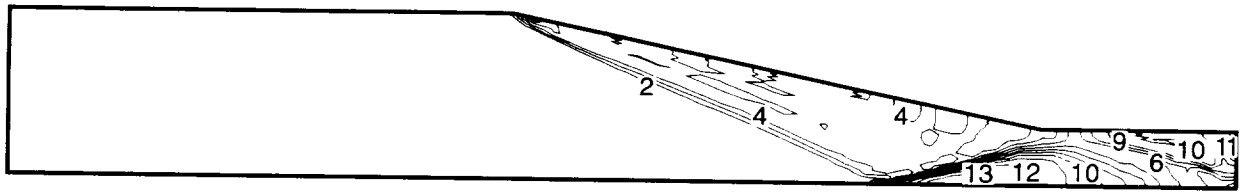

(c) $Z/H = 0.75$.

Figure 5. Contours of p/p_∞ in horizontal planes for 0 percent cowl. CR = 3; Re = 2.15×10^6 per foot.

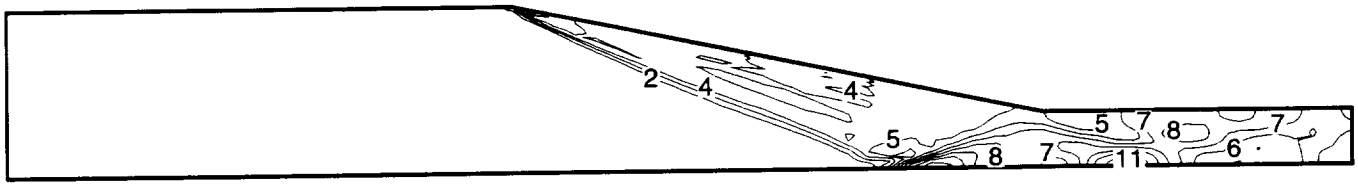

(a) $Z/H = 0.25$.

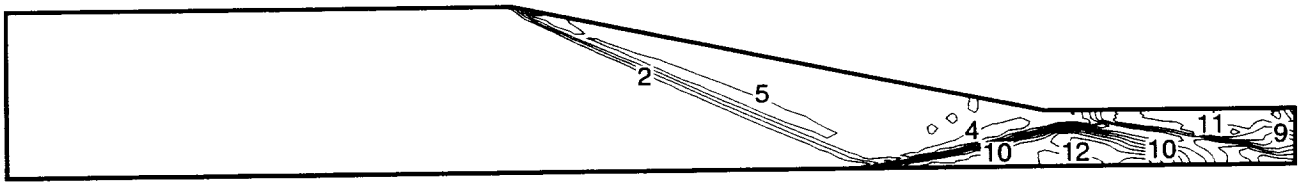

(b) $Z/H = 0.50$.

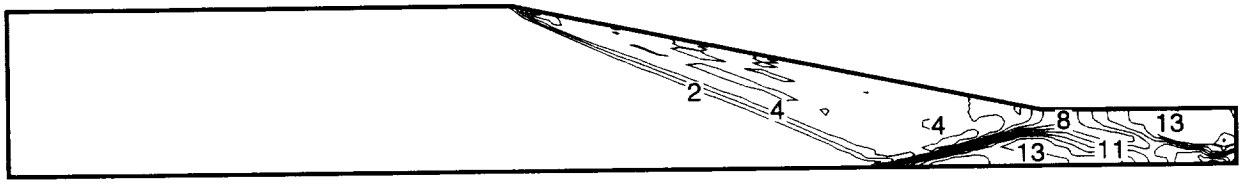

(c) $Z/H = 0.75$.

Figure 6. Contours of p/p_∞ in horizontal planes for 50 percent cowl. CR = 3; Re = 2.15×10^6 per foot.

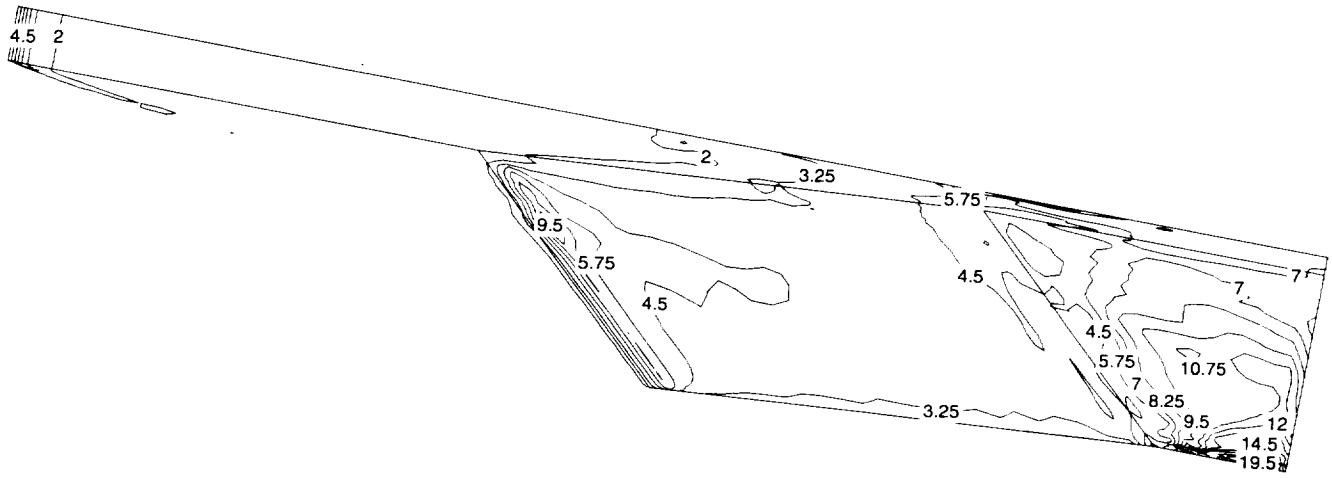

Figure 7. Contours of p/p_∞ on inlet sidewall and baseplate for 0 percent cowl. CR = 3; Re = 2.15×10^6 per foot.

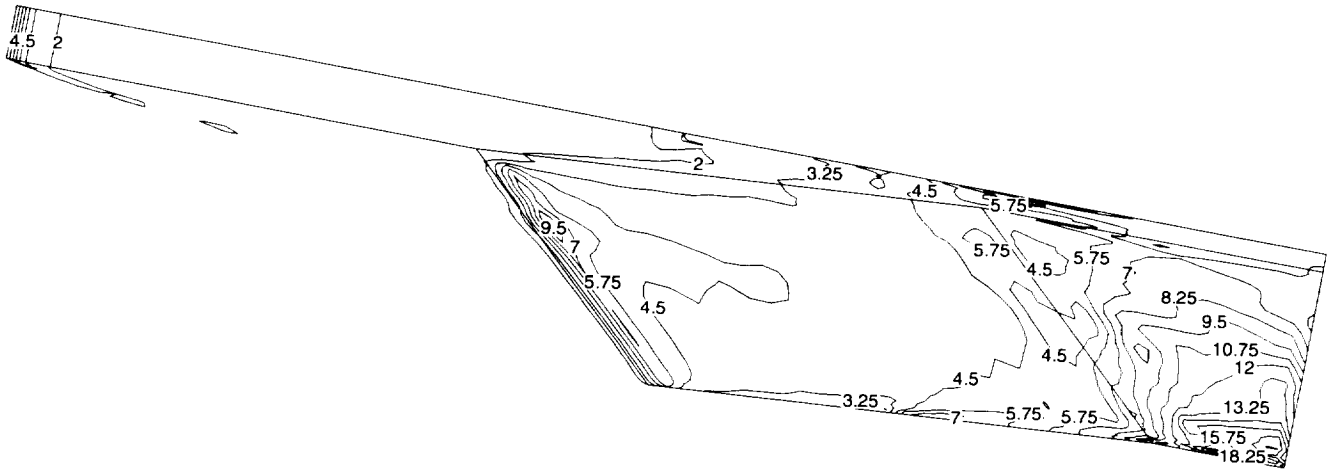

Figure 8. Contours of p/p_∞ on inlet sidewall and baseplate for 50 percent cowl. CR = 3; Re = 2.15×10^6 per foot.

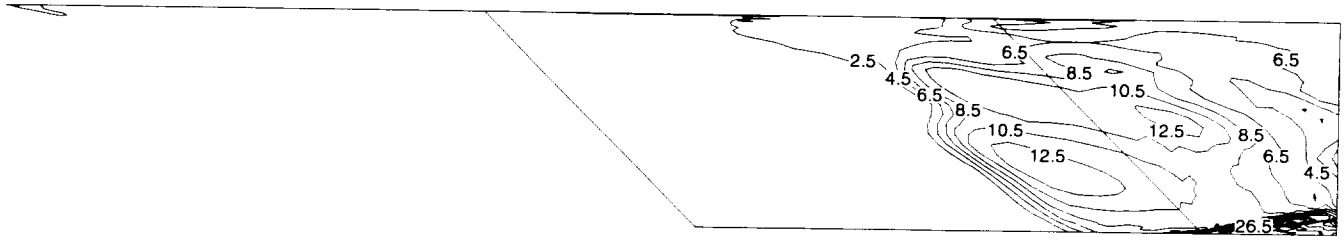

Figure 9. Contours of p/p_∞ on inlet symmetry plane for 0 percent cowl. CR = 3; Re = 2.15×10^6 per foot.

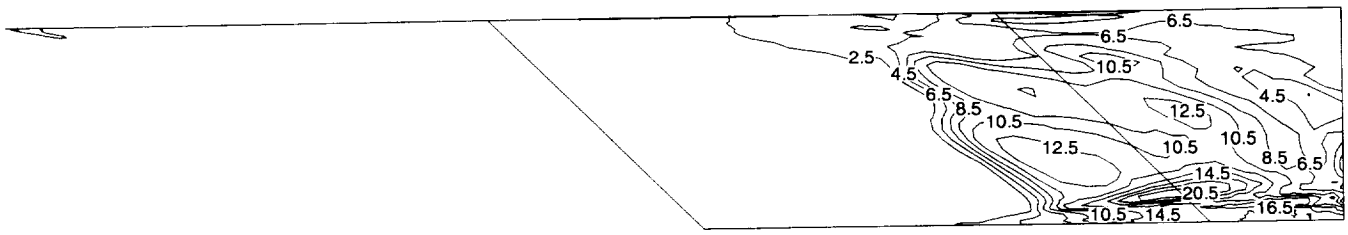

Figure 10. Contours of p/p_∞ on inlet symmetry plane for 50 percent cowl. CR = 3; Re = 2.15×10^6 per foot.

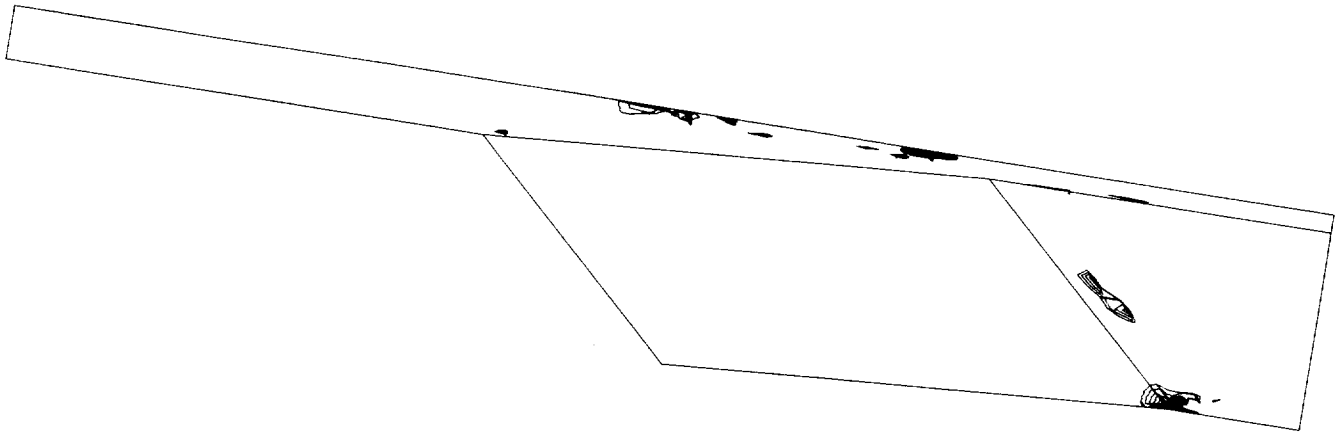

Figure 11. Axial separation regions on inlet sidewall and baseplate for 0 percent cowl. CR = 3; Re = 2.15×10^6 per foot.

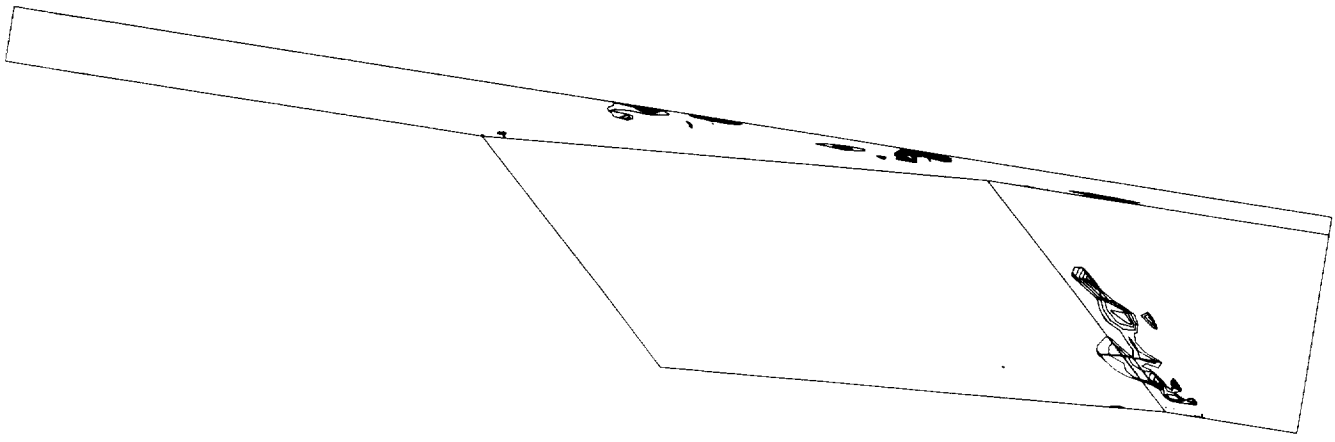

Figure 12. Axial separation regions on sidewall and baseplate for 50 percent cowl. CR = 3; Re = 2.15×10^6 per foot.

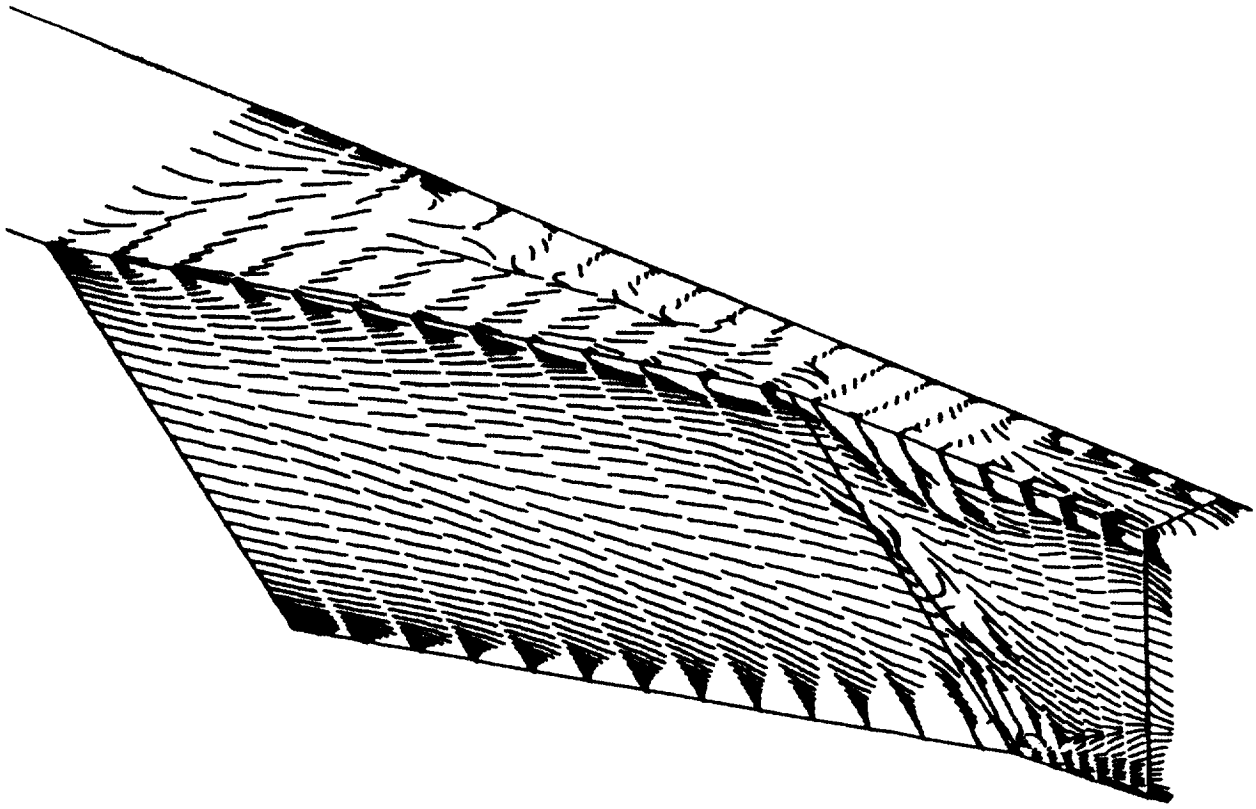

Figure 13. Simulated oil flow for 0 percent cowl. CR = 3; Re = 2.15×10^6 per foot.

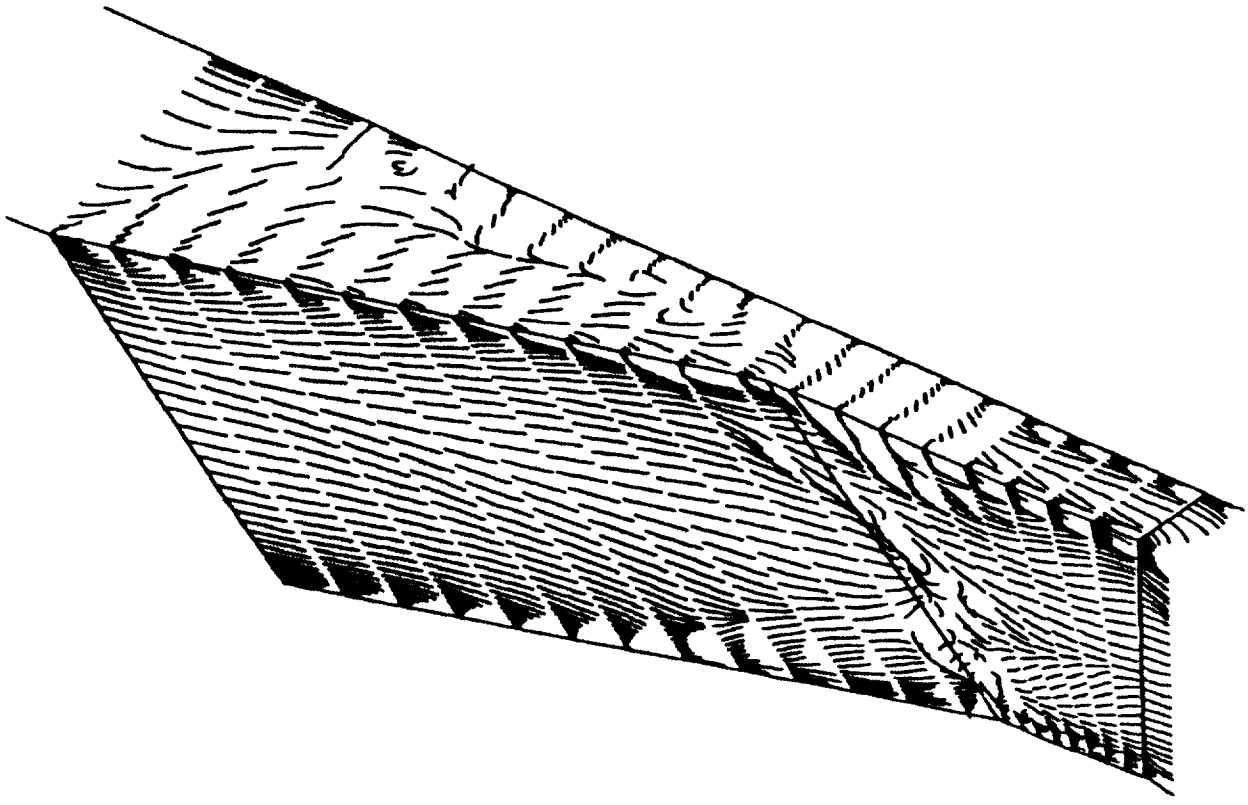

Figure 14. Simulated oil flow for 50 percent cowl. CR = 3; Re = 2.15×10^6 per foot.

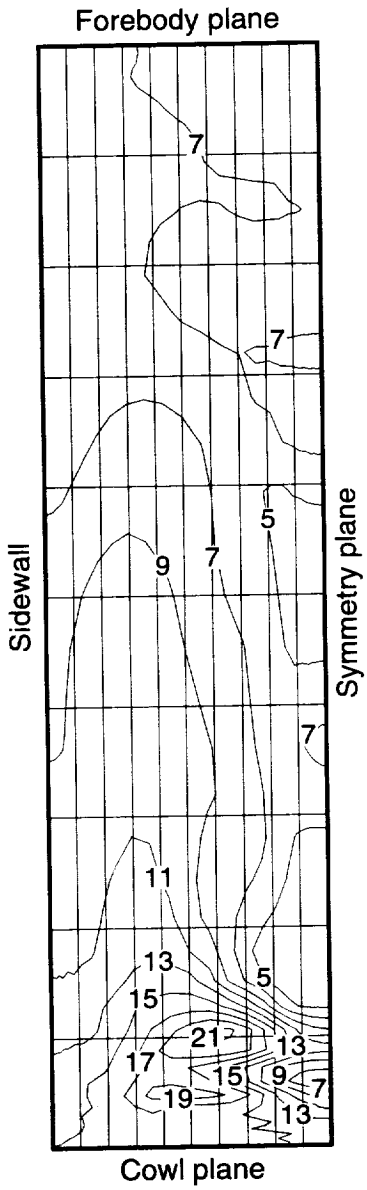

Figure 15. Contours of p/p_∞ in exit plane of constant-area throat ($i = 72$) for 0 percent cowl. CR = 3; Re = 2.15×10^6 per foot.

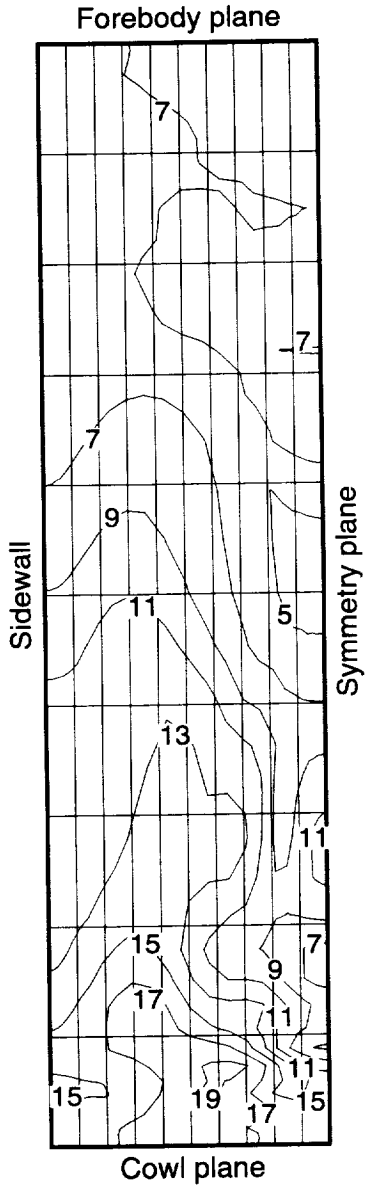

Figure 16. Contours of p/p_∞ in exit plane of constant-area exit ($i = 72$) for 50 percent cowl. CR = 3; Re = 2.15×10^6 per foot.

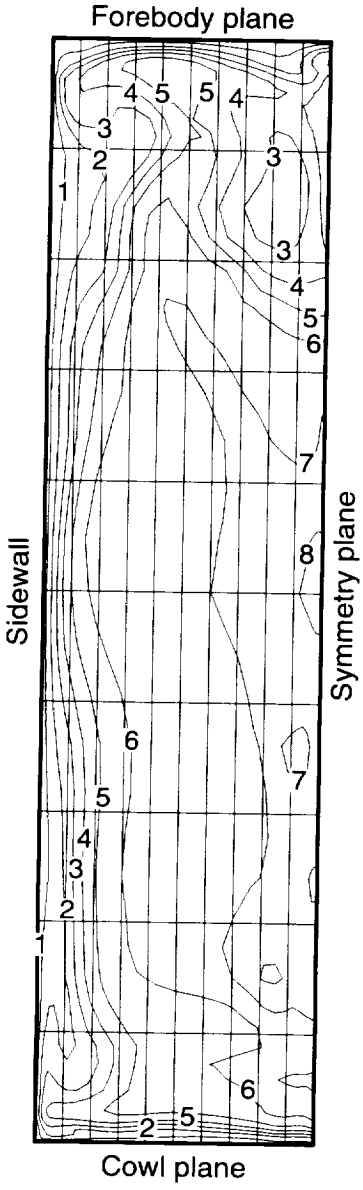

Figure 17. Exit plane Mach number for 0 percent cowl. CR = 3; Re = 2.15×10^6 per foot.

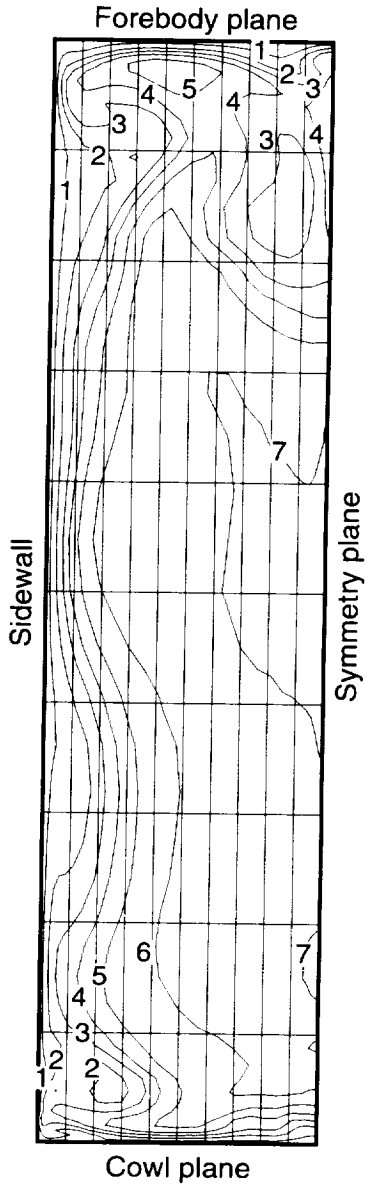

Figure 18. Exit plane Mach number for 50 percent cowl. CR = 3; Re = 2.15×10^6 per foot.

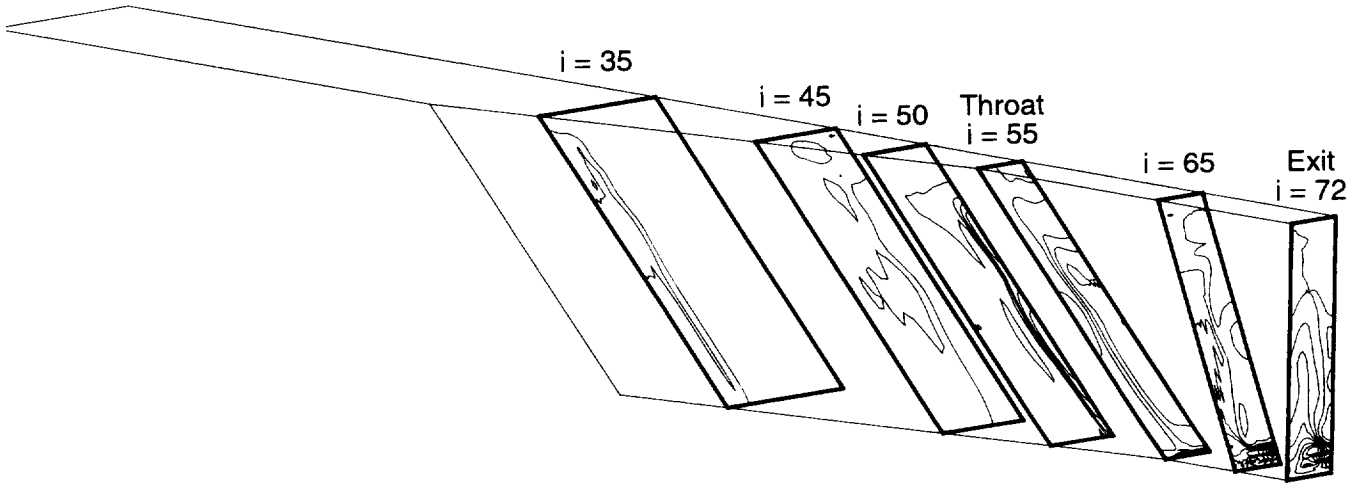

Figure 19. Composite of p/p_∞ contours in i = Constant planes for 0 percent cowl. CR = 3; Re = 2.15×10^6 per foot.

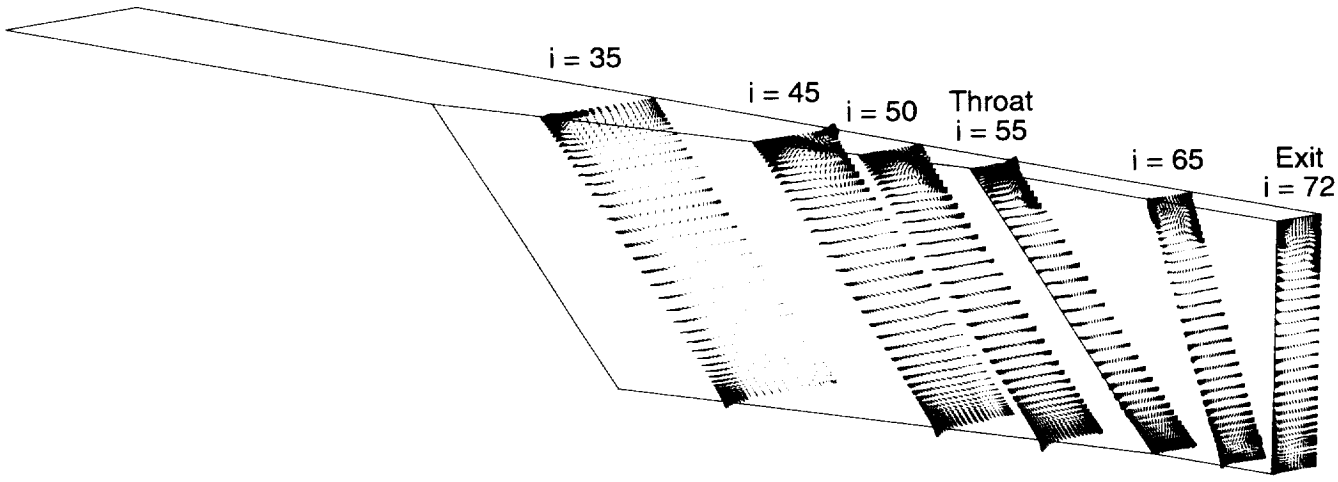

Figure 20. Composite of velocity vectors in i = Constant planes for 0 percent cowl. CR = 3; Re = 2.15×10^6 per foot.

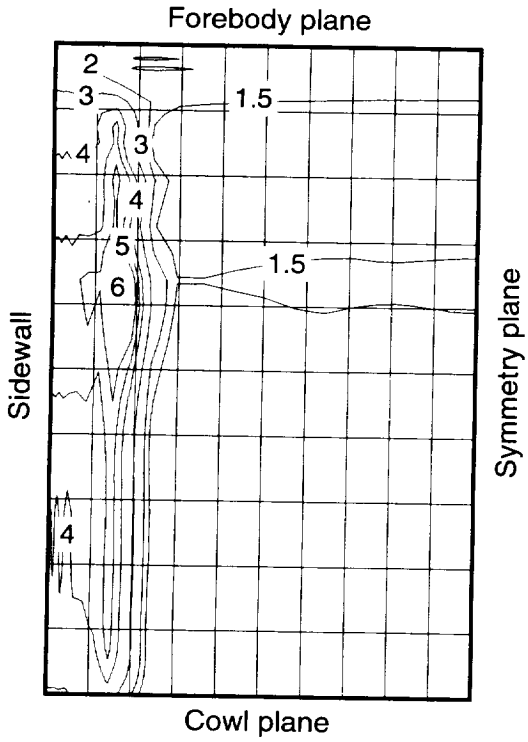

(a) $i = 35$; $x'/T_x' = 0.20$.

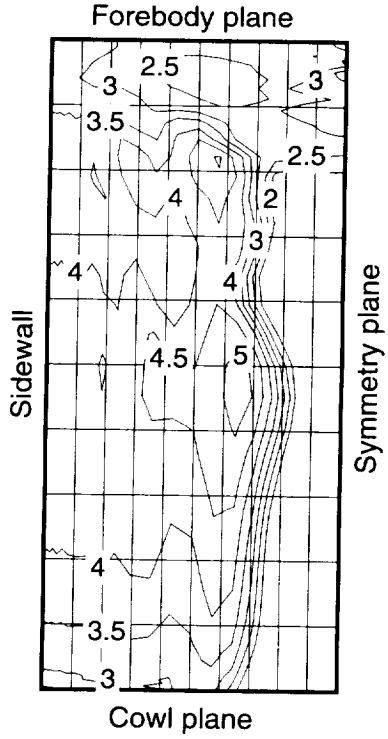

(b) $i = 45$; $x'/T_x' = 0.60$.

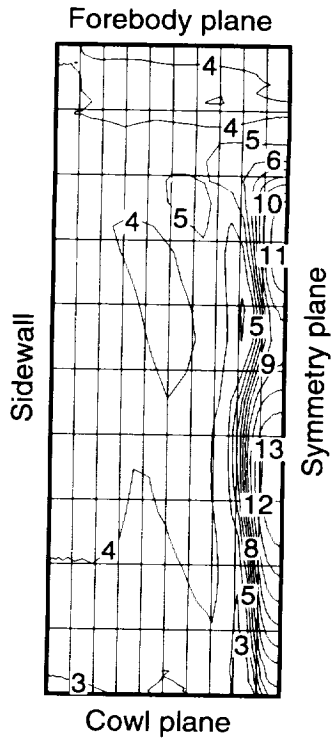

(c) $i = 50$; $x'/T_x' = 0.79$.

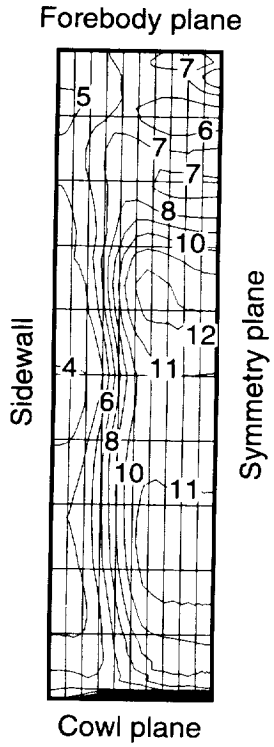

(d) $i = 55$; $x'/T_x' = 1.00$.

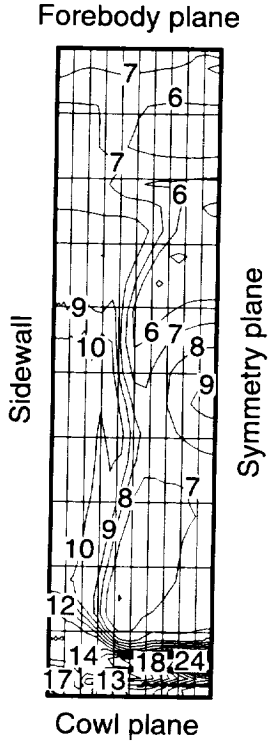

(e) $i = 65$.

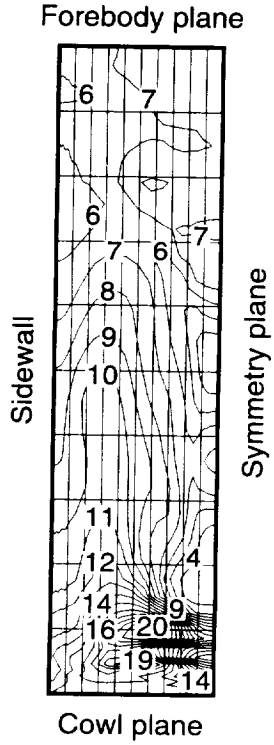

(f) $i = 72$; exit.

Figure 21. Contours of p/p_∞ in i = Constant planes for 0 percent cowl. CR = 3; Re = 2.15×10^6 per foot.

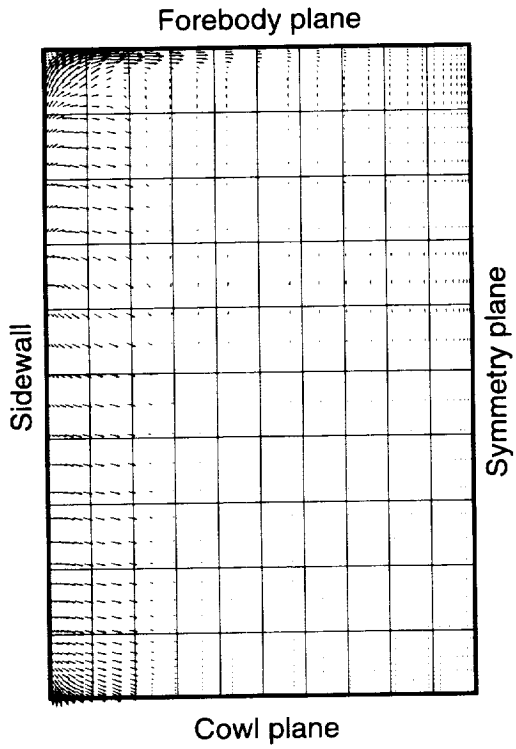

(a) $i = 35$; $x'/T_x' = 0.20$.

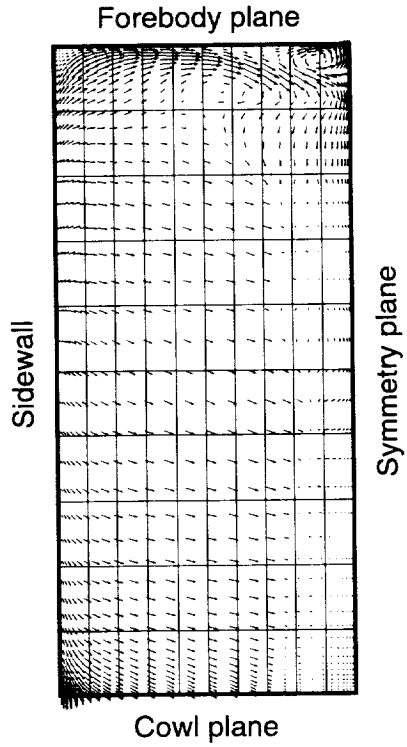

(b) $i = 45$; $x'/T_x' = 0.60$.

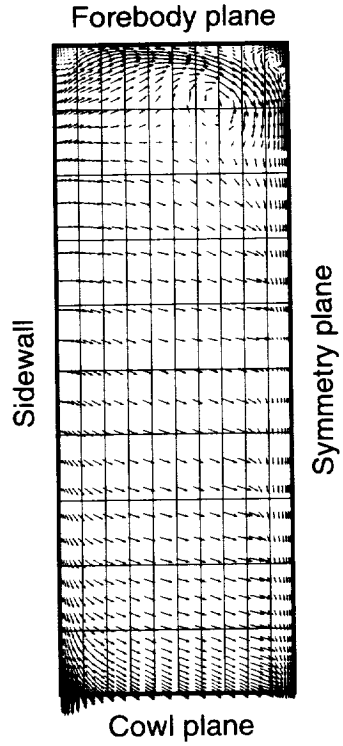

(c) $i = 50$; $x'/T_x' = 0.79$.

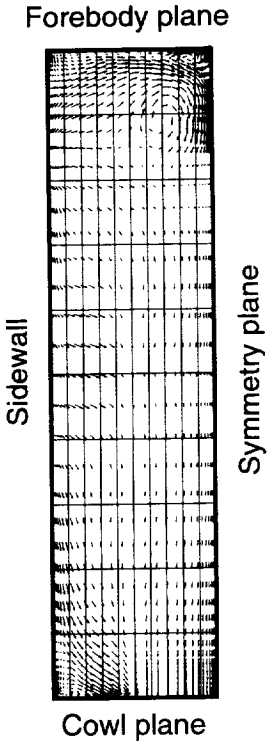

(d) $i = 55$; $x'/T_x' = 1.00$.

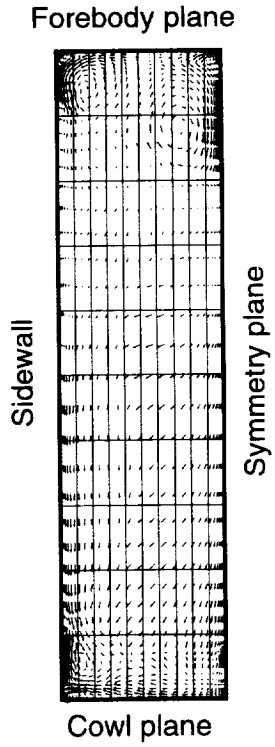

(e) $i = 65$.

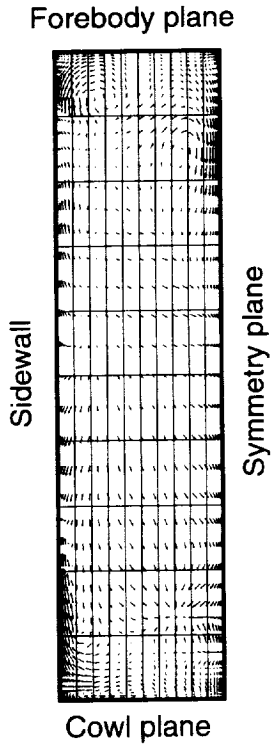

(f) $i = 72$; exit.

Figure 22. Velocity vectors v, w in i = Constant planes for 0 percent cowl. CR = 3; Re = 2.15×10^6 per foot.

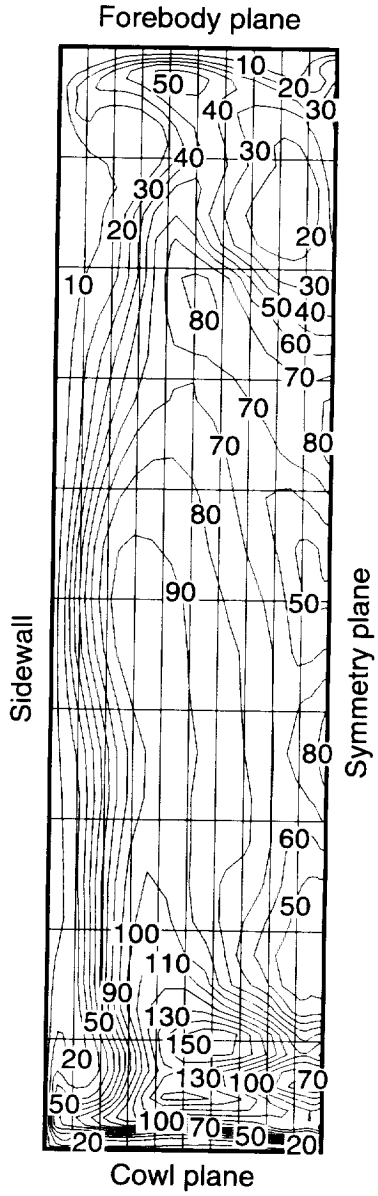

Figure 23. Mass flux contours, in kg/m^{2}s, in exit plane (i = 72) for 0 percent cowl. CR = 3; Re = 2.15×10^6 per foot.

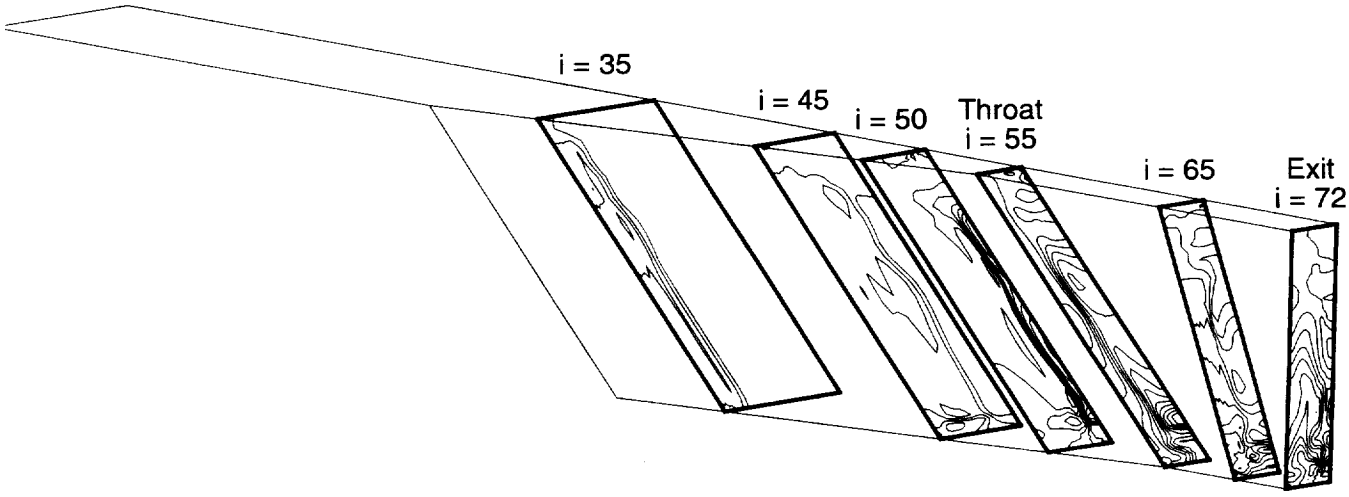

Figure 24. Composite of p/p_∞ contours in i = Constant planes for 50 percent cowl. CR = 3; Re = 2.15×10^6 per foot.

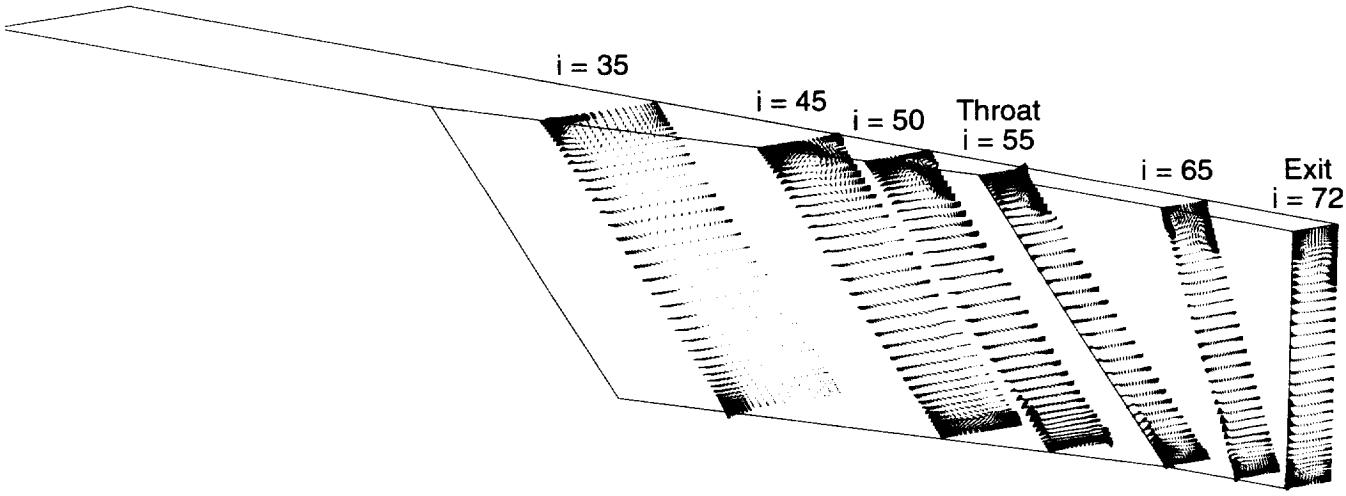

Figure 25. Composite of v, w velocity vectors in i = Constant planes for 50 percent cowl. CR = 3; Re = 2.15×10^6 per foot.

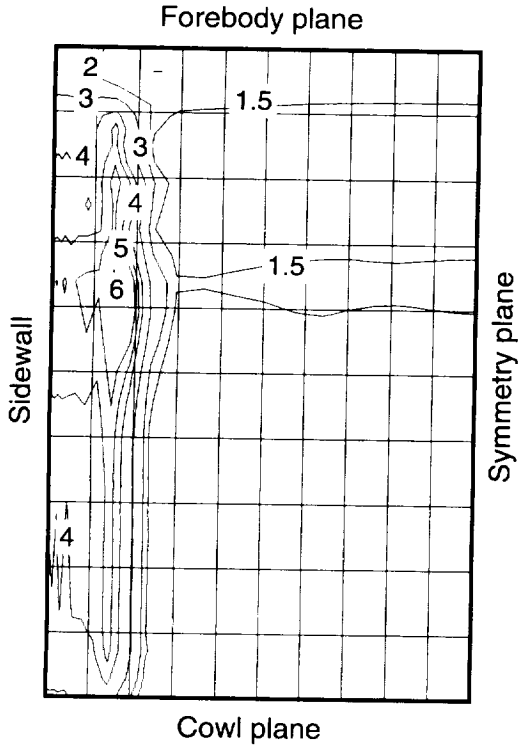

(a) $i = 35$; $x'/T_x' = 0.20$.

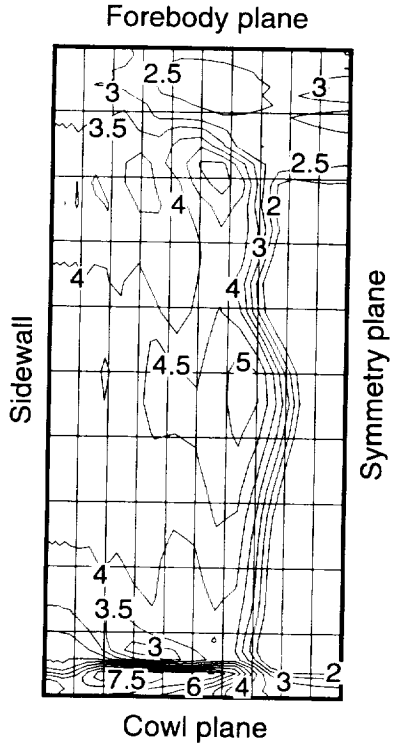

(b) $i = 45$; $x'/T_x' = 0.60$.

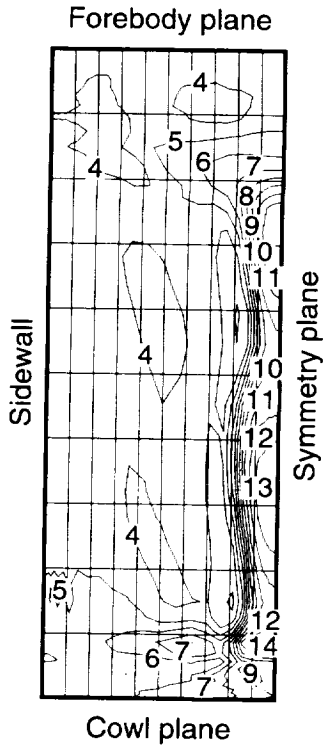

(c) $i = 50$; $x'/T_x' = 0.79$.

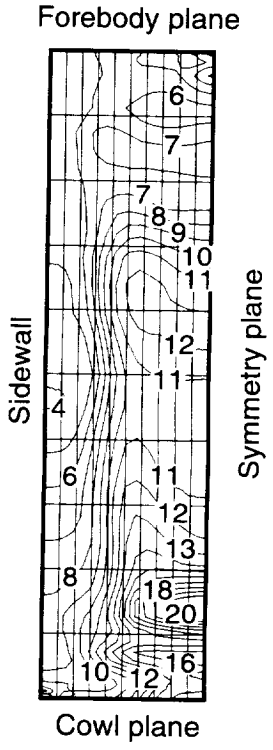

(d) $i = 55$; $x'/T_x' = 1.00$.

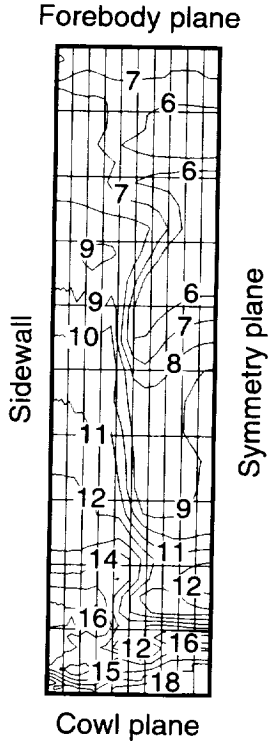

(e) $i = 65$.

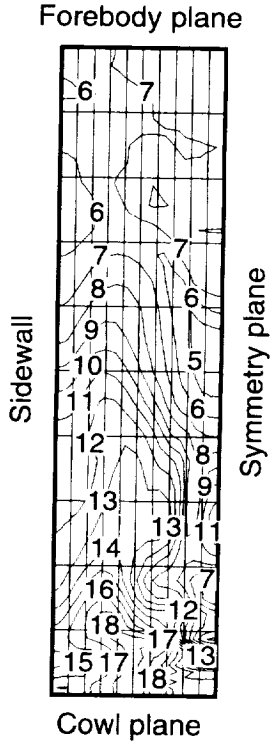

(f) $i = 72$; exit.

Figure 26. Contours of p/p_∞ in i = Constant planes for 50 percent cowl. CR = 3; Re = 2.15×10^6 per foot.

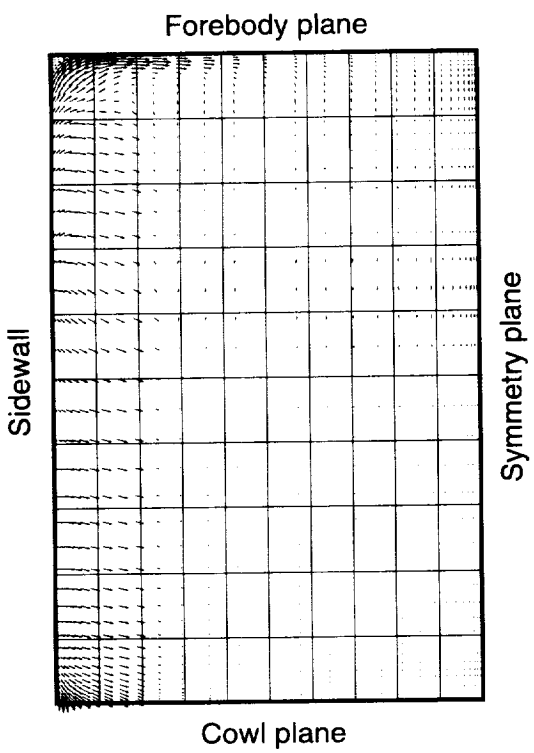

(a) $i = 35$; $x'/T_x' = 0.20$.

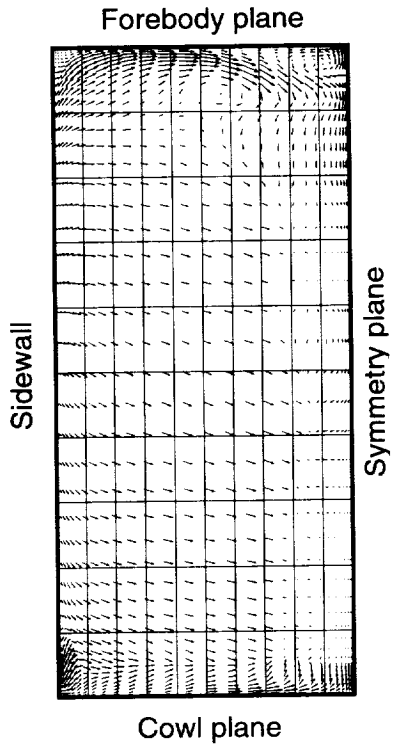

(b) $i = 45$; $x'/T_x' = 0.60$.

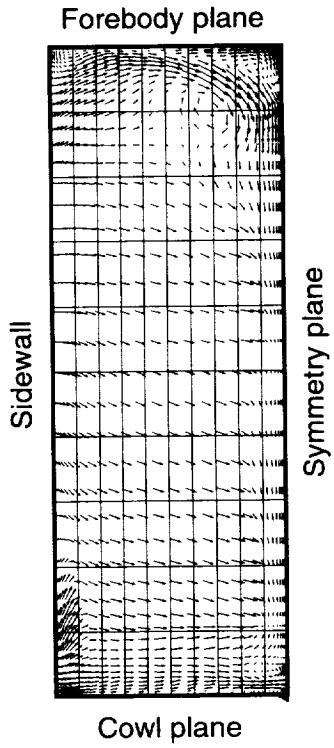

(c) $i = 50$; $x'/T_x' = 0.79$.

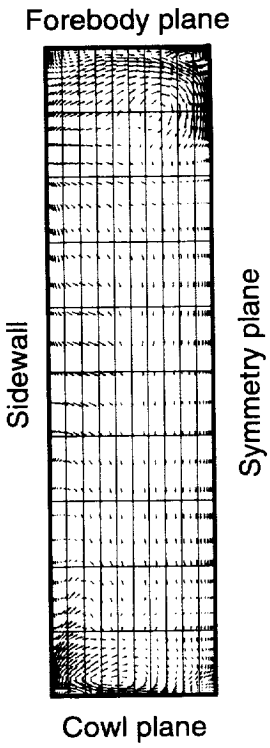

(d) $i = 55$; $x'/T_x' = 1.00$.

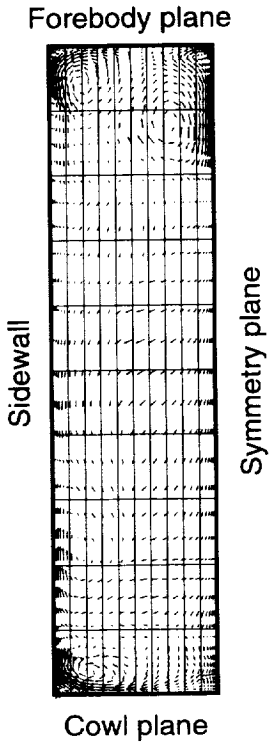

(e) $i = 65$.

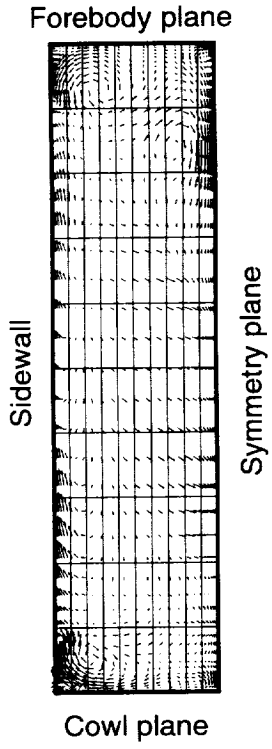

(f) $i = 72$; exit.

Figure 27. Velocity vectors v, w in i = Constant planes for 50 percent cowl. CR = 3; Re = 2.15×10^6 per foot.

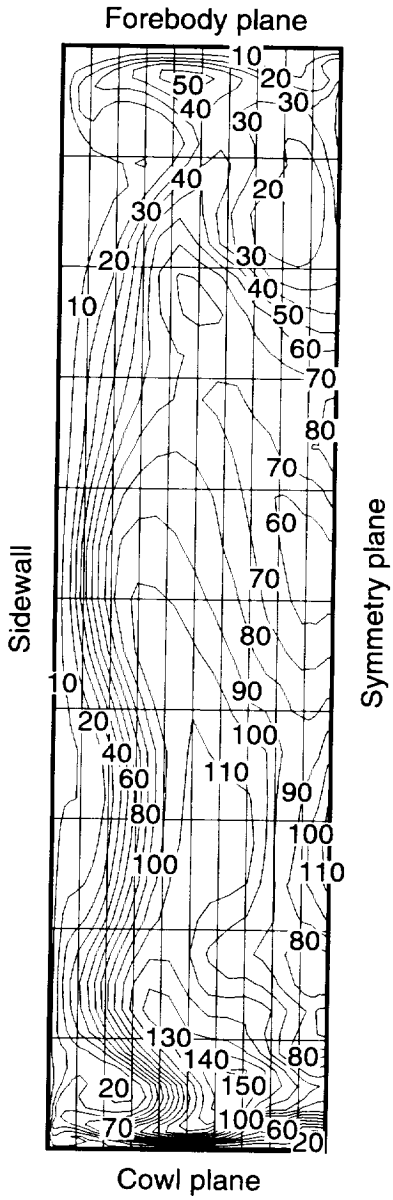

Figure 28. Mass flux contours, in kg/m^{2}s, in exit plane (i = 72) for 50 percent cowl. CR = 3; Re = 2.15×10^6 per foot.

REPORT DOCUMENTATION PAGE

Form Approved
OMB No. 0704-0188

1. AGENCY USE ONLY *(Leave blank)*	2. REPORT DATE	3. REPORT TYPE AND DATES COVERED
	March 1995	Technical Memorandum

4. TITLE AND SUBTITLE
Mach 10 Computational Study of a Three-Dimensional Scramjet Inlet Flow Field

5. FUNDING NUMBERS
WU 506-40-41-02

6. AUTHOR(S)
Scott D. Holland

7. PERFORMING ORGANZATION NAME(S) AND ADDRESS(ES)
NASA Langley Research Center
Hampton, VA 23681-0001

8. PERFORMING ORGANIZATION REPORT NUMBER
L-17348

9. SPONSORIING/MONITORING AGENCY NAME(S) AND ADDRESS(ES)
National Aeronautics and Space Administration
Washington, DC 20546-0001

10. SPONSORING/MONITORING AGENCY REPORT NUMBER
NASA TM-4602

11. SUPPLEMENTARY NOTES

12a. DISTRIBUTION/AVAILABILITY STATEMENT
Unclassified–Unlimited
Subject Category 34
Availability: NASA CASI (301) 621-0390

12b. DISTRIBUTION CODE

13. ABSTRACT *(Maximum 200 words)*
The present work documents the computational results for a combined computational and experimental parametric study of the internal aerodynamics of a generic three-dimensional sidewall-compression scramjet inlet configuration at Mach 10. The three-dimensional Navier-Stokes code SCRAMIN was chosen for the computational portion of the study because it uses a well-known and well-proven numerical scheme and has shown favorable comparison with experiment at Mach numbers between 2 and 6. One advantage of CFD was that it provided flow field data for a detailed examination of the internal flow characteristics in addition to the surface properties. The experimental test matrix at Mach 10 included three geometric contraction ratios (3, 5, and 9), three Reynolds numbers (0.55×10^6 per foot, 1.14×10^6 per foot, and 2.15×10^6 per foot), and three cowl positions (at the throat and two forward positions). Computational data for two of these configurations (the contraction ratio of 3, $Re = 2.15 \times 10^6$ per foot, at two cowl positions) are presented along with a detailed analysis of the flow interactions in successive computational planes.

14. SUBJECT TERMS
Hypersonics; Inlets; Computational fluid dynamics (CFD); Shock interactions

15. NUMBER OF PAGES
30

16. PRICE CODE
A03

17. SECURITY CLASSIFICATION OF REPORT	18. SECURITY CLASSIFICATION OF THIS PAGE	19. SECURITY CLASSIFICATION OF ABSTRACT	20. LIMITATION OF ABSTRACT
Unclassified	Unclassified	Unclassified	

NSN 7540-01-280-5500

Standard Form 298 (Rev. 2-89)
Prescribed by ANSI Std. Z39-18
298-102